A New Monte-Carlo Based Simulation for the CryoEDM Experiment

Matthew Rásó-Barnett

Submitted for the degree of Master of Philosophy
School of Mathematical and Physical Sciences
University of Sussex
September 2013
Supervisors: Dr S J M Peeters and Prof P G Harris

Declaration

I hereby declare that this thesis describes my own original work, except where explicitly stated. No part of this work has previously been submitted, either in the same or different form, to this or any other University in connection with a higher degree or qualification.

Matthew Rásó-Barnett

Signed:

Date: March 26, 2015

University of Sussex

Matthew Rásó-Barnett, Master of Philosophy

A new Monte-Carlo based simulation for the CryoEDM Experiment

Abstract

This thesis presents a new Monte-Carlo based simulation of the physics of ultra-cold neutrons (UCN) in complex geometries and its application to the CryoEDM experiment. It includes a detailed description of the design and performance of this simulation along with its use in a project to study the magnetic depolarisation time of UCN within the apparatus due to magnetic impurities in the measurement cell, which is a crucial parameter in the sensitivity of a neutron electric-dipole-moment (nEDM) experiment. This project involved experimental measurements taken at the Institut Laue Langevin (ILL) of the magnetic environment inside of CryoEDM's measurement cell, along with the magnetic field produced by a set of 19 coils around the cell used to optimise the field in particular locations. It also involved the development of a separate computer program to find the required current setting of these coils so as to minimise the field gradient across the measurement cell, and then use of the simulation to study the effect of these coil configurations on the magnetic depolarisation time.

Contents

Acknowledgements

I've been incredibly fortunate to have had the support of so many people throughout my time at Sussex, without whom I wouldn't have finished. It hasn't been the easiest or most successful of periods, however I've learned a lot and I'm glad that I've been here and had the chance to work with so many incredible people at Sussex.

I would first like to thank my wife Lívia, who has put up with me struggling through this for 5 years and didn't let me throw it all away. Her support has been invaluable and I apologise for putting her through it.

I'd also like to thank my supervisor, Dr Simon Peeters especially, for supporting me. He has been extraordinarily patient and understanding with me and gave me the push and encouragement to keep going and hand this in when I thought I would surely give up.

I am really grateful for all of the advice and help given to me over the years by the CryoEDM team at Sussex, especially from my second supervisor Professor Philip Harris and Professor Mike Hardiman.

Lastly, it wouldn't have been anywhere as near as good a time without my fellow students Aikaterini Katsika, Andrew Davidson, Nicholas Devenish and Shakeel Fernandes. You were all great friends and I'm glad we had the chance to study together.

1 Introduction

The Universe started with the Big Bang. Our current understanding of particle physics suggests that in this process, an equal amount of particles and anti-particles were produced. Although antimatter can be created in a laboratory or in the upper atmosphere, as a result of a comic shower, there is no evidence of anti-matter planets, galaxies or elsewhere in the Universe.

There is apparently a small asymmetry between the reactions of matter and anti-matter, which caused that there is matter left in the Universe today, while most matter and anti-matter has been annihilated. The mechanism in particle physics creating such an asymmetry is so-called CP-violation.

The neutron Electric Dipole Moment (nEDM) is an extremely sensitive way to directly test the presence of CP asymmetry in nature.

After this introduction chapter, chapter 2 of this thesis describes the nEDM and the current experiment status, as well as the CryoEDM experiment, which is the focus of this thesis and the physics involved with the measurement of the nEDM.

Chapter 3 of this thesis describes in detail the development of a new Monte-Carlo simulation for ultra-cold neutron (UCN) experiments. This Monte-Carlo only relies on the ROOT framework for the handling and visualisation of the geometry. It can propagate UCN in a complex

geometry and any combination of electric and magnetic environment. It describes the verification that has been done on this software. This Monte-Carlo is entirely the author's own work and it has become the default simulation tool for the CryoEDM experiment.

Chapter 4 describes the optimisation of the magnetic field for the CryoEDM experiment. This directly influence the sensitivity that can be reached of the CryoEDM experiment. The work was lead by the author, and the fitting program to find the optimal currents for the 19 coils. It then describes the effect of this optimisation on the physics performance of the experiment.

The thesis ends with a short conclusion, including suggestions for further work.

2 Neutron Electric Dipole Moment and the CryoEDM Experiment

2.1 The Neutron EDM

The neutron was discovered by Chadwick (1932) and was the last of the three atomic particles to be found. Prior to this, the popular belief was that the only particles present in the atom and atomic nucleus were the proton and the electron. This hypothesis had problems, for example, the observed spin of ^{14}C could not be satisfied by any combination of protons and electrons. When, in 1920 Rutherford predicted the existence of a nuclear particle with mass approximately that of the proton but electrically neutral, the search was on to find this particle. Chadwick had discovered the neutron and was awarded the Nobel Prize in Physics in 1935. The neutron is now very well understood: it has a mass of : 1.00866491578(55) amu and is not an elementary particle but made from 1 up ($+2/3e$) and two down quarks ($-1/3e$ and $-1/3e$), and has an overall charge of zero. The moment and spin of the quarks within the neutron contribute to give it a spin 1/2 and magnetic dipole moment μ_n of -1.91 μ_N, where μ_N is the nuclear magneton equal to,

$$\mu_n = \frac{e\hbar}{2m_p} \tag{2.1}$$

where m_p stands for the proton rest mass.

One property that has been predicted but not found to date is the

neutron electric dipole moment (nEDM). Although the overall charge of the neutron is zero, if the centres of the positive and negative charge do not coincide, this will give rise to an electric dipole moment (EDM) [1]. The EDM is defined as the distance separating the centres of mass of the positive and negative charges multiplied by the magnitude of their charge, in the direction of the spin axis. This can be written as:

$$d_n = x \cdot q \tag{2.2}$$

where d_n is the nEDM, x is the distance separating the centres of charge and q the magnitude of the charge.

2.2 Constraining the Neutron EDM Experimentally

From dimensional requirements [2] predicts the magnitude of a nEDM (d_n) arising from second order interaction in the standard model is,

$$d_n \sim e\frac{G_F^2}{\pi^4}\frac{m_t^2}{M_W^2}\Im\Delta^{(4)}\mu^3 \approx 10^{-31}e \cdot \text{cm}, \tag{2.3}$$

where $\Im\Delta^{(4)} = A^2\lambda^2\eta = c_1c_2c_3s_1^2s_2s_3 \sim 10^{-4}$ is a required CP violating factor. The terms A, λ, η are terms from the Wolfenstein CKM matrix and c_i and s_i are the cos and sin of the mixing angles of CKM matrix. The term $\frac{m_t^2}{M_W^2}$ comes from the GIM mechanism. The factor π is included from loop diagrams and μ is the typical hadronic scale (0.3 GeV) making the term dimensionally correct. This predicted value for a permanent nEDM of $10^{-31}e \cdot \text{cm}$ is well outside any current experimental measurements. However, many other theories have predicted nEDM values which will be explored in the next generation of nEDM experiments. Indeed since Ramsey's first publication [3] of the upper limit of the neutron EDM in 1957 of $5 \times 10^{-20}e \cdot \text{cm}$ the current upper limit has been improved experimentally by ~ 6 orders of magnitude, as shown in Fig.2.1. The current upper limit, held by

the Sussex-RAL collaboration, is $2.9 \times 10^{-26} e \cdot \text{cm}$ [4]. The next generation of nEDM experiments should be capable of reducing the upper limit to $10^{-28} e \cdot \text{cm}$. One theory outside the standard model which is being increasingly put under pressure by improving nEDM upper limits is Supersymmetry. In the supersymmetric model the addition of superpartners for all fermions and bosons allows one loop contributions to quark EDMs, producing an nEDM in the range from 10^{-23} to $10^{-24} e \cdot \text{cm}$. These values disagree with experiment by orders of magnitude. However, a minimal supersymmetric model predicts an nEDM of order 10^{-27} to $10^{-25} e \cdot \text{cm}$ [5].

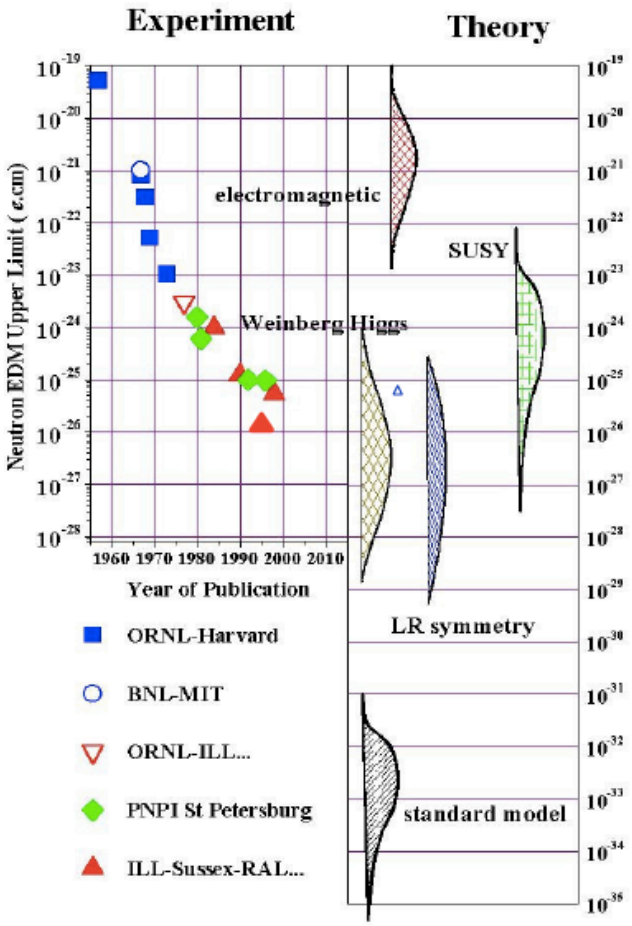

Figure 2.1: The experimental upper limit set on the Neutron electric dipole moment (nEDM) as a function of the year of publication. Included is the ILL-Sussex-RAL current upper limit of $2.9 \times 10^{-26} e \cdot \text{cm}$. Also shown on the right hand side are theoretical predictions of the nEDM.

This should be within the range of the next generation of nEDM experiments. If a nEDM is observed at this level it will be a direct

observation of physics beyond the standard model. Many theories predict a nEDM to be approximately of this magnitude as a nEDM of this magnitude is thought to be needed to explain the extent of the baryon asymmetry of the Universe.

2.3 The Interactions of Ultra Cold Neutrons

In this section, the interaction of ultra-cold neutrons (UCN) will be described. UCN are free neutrons of such low kinetic energy that they can be stored in containers made from certain materials such that UCN reflect from the material under any angle of incidence. This can be done by exploiting materials with a high Fermi-potential, an effective potential due to the interaction of cold neutrons with many atoms. The strong interaction is responsible for this and neutron interactions governed by this force will be described first. Next, the weak interaction, responsible for the finite lifetime of the neutron will be described.

The material in this chapter is largely based on material from [6].

2.3.1 The Strong Interaction

2.3.1.1 Scattering from a Single Nucleus

The interaction of a slow neutron and a proton can be adequately described by an attractive spherical square-well potential, with a depth $V_0 = 40$ MeV and a radius, $R \sim 2\times10^{-15}$ m. For larger nuclei the force is much the same, with the well depth remaining nearly constant. For slower/lower energy neutrons, the scattering from this potential becomes predominantly S-wave (orbital angular momentum, $l = 0$) and independent of the details of the attractive potential. Indeed, at low

enough energies the scattering is characterised by a single parameter known as the *scattering length* [7]. The total wavefunction outside the well (incident plus scattered wave) is,

$$\psi = e^{i\mathbf{k}\cdot\mathbf{r}} + f(\theta)\frac{e^{ikr}}{r} \quad \text{for} \quad r > R_n \tag{2.4}$$

where the first term represents the incident plane wave, the second term represents a scattered spherical wave centred on the nucleus and R_n is the size of the nuclear potential well. The function $f(\theta)$ is called the scattering amplitude and contains all the details about the interaction between the neutron and nuclear potential.

Partial wave analysis shows that the scattering amplitude at low energy, where the de Broglie wavelength for the neutron is much greater than the range of the interaction R is:

$$f(\theta) = -a, \tag{2.5}$$

where a is the scattering length.

In general, the scattering length a depends on the relative orientation of the neutron and nuclear spin. Averaging a over all possible orientations between neutron and nuclear spin, which is what we are interested in since the nuclei in the wall-material should be unpolarised, gives the 'coherent' scattering length, which is what we will refer to by a in future.

2.3.1.2 The Fermi Potential: Scattering from a Collection of Nuclei

Since the energy of cold neutrons is much lower than the nuclear potential ($\approx$ 40 MeV), the neutron wavefunction will be very different within range of the nuclear potential than far from it. Therefore, the Born Approximation (Perturbation theory) is not suitable to describe the scattering. However, Fermi realised that one could introduce an

effective pseudo-potential which could be used in the Born approximation to calculate the changes to the neutron wavefunction outside the range of the nuclear potential.

The Born approximation gives an expression for the scattering amplitude when the energy of the incident particle is larger than the scattering potential:

$$f(\theta,\phi) = -\frac{\mu}{2\pi\hbar^2}\int V(\mathbf{r})e^{i(\mathbf{k}_i-\mathbf{k}_f)\cdot\mathbf{r}}d^3r, \tag{2.6}$$

where, $V(\mathbf{r})$ is the scattering potential, μ is the reduced mass, and $\mathbf{k}_i, \mathbf{k}_f$ are the incident and final wave-vectors. By substituting the low energy result from partial wave analysis (2.5) into the Born approximation we get,

$$a = \frac{\mu}{2\pi\hbar^2}\int U_F(\mathbf{r})e^{i(\mathbf{k}_i-\mathbf{k}_f)\cdot\mathbf{r}}d^3r \tag{2.7}$$

and thus a solution for U_F, Fermi's psuedo-potential is:

$$U_F(\mathbf{r}) = \frac{2\pi\hbar^2 b}{m}\delta^3(\mathbf{r}), \tag{2.8}$$

where m is the neutron mass and b is the *bound-coherent scattering length*, given by $b = \frac{m}{\mu}a$.

Inside a material there are many nuclei, each with their own scattering potential given by 2.8, and so a neutron incident on this material would average over the volume of these δ-function potentials. This gives:

$$V_F = \frac{2\pi\hbar^2}{m}\sum_i N_i b_i, \tag{2.9}$$

where N_i is the number of nuclei per unit volume of nuclear species i. This potential is commonly referred to as the material's Mean Fermi Potential, or usually just Fermi Potential for short.

2.3.1.3 Total Reflection of Neutrons from Material Walls

One of the first and most crucial aspects of UCN physics to all experiments is to clarify how UCN can be reflected from a material surface, such as a neutron guide tube, since this is the dominant interaction for all neutron storage experiments. For such a large, macroscopic object, the wall of a neutron guide tube is effectively an infinite one-dimensional surface to an incoming neutron, and thus the problem can be treated as particle reflection from a one-dimensional potential boundary.

Considering for a moment the neutron as a classical particle, it is obvious why reflection occurs. When a neutron of kinetic energy $E_\perp$ penetrates the material, it acquires a potential energy V_F and therefore its kinetic energy becomes $E_\perp - V_F$, where V_F is the mean fermi potential of the material given by 2.9. From energy conservation, it follows that if the incident neutron energy is smaller than the potential $E_\perp < E_{crit} = V_F$, then the neutron cannot penetrate the material. Thus neutrons approaching the material at small grazing angles such that $E_\perp < E_{crit}$ will be totally reflected from the surface of the material. Neutrons with total kinetic energy E less than E_{crit} will be reflected at all angles of incidence, and as such can be stored in a closed container.

Quantum mechanically, this process can be shown as a one-dimensional quantum mechanical wave incident on a potential step, familiar from many introductory texts. Particles with $E_\perp < V_F$ will similarly be reflected, but there is also some finite probability that the particle will penetrate the potential step by a small amount. Likewise, there is also a probability of reflection for particles with $E_\perp > V_F$.

If we consider a one-dimensional potential step, V extending from

$x > 0$, the wave-function will be of the form:

$$\psi = \begin{cases} e^{ikx} + Re^{-ikx} \quad \text{where,} \quad k^2 = \frac{2mE}{\hbar^2} & (x < 0) \\ Te^{ik'x} \quad \text{where,} \quad k'^2 = \frac{2m(E-V)}{\hbar^2} & (x > 0) \end{cases}, \tag{2.10}$$

where for $x < 0$ the first term of the wave-function represents the incident wave and the second term is the reflected wave of amplitude R. This corresponds to a net probability current or *flux* moving in the positive x-direction, of magnitude,

$$\begin{aligned} j(x,t) &\equiv \frac{\hbar}{2im}\left(\psi^* \frac{\partial \psi}{\partial x} - \frac{\partial \psi^*}{\partial x}\psi\right) \\ &= \frac{\hbar k}{m}\left(1 - |R|^2\right) \end{aligned} \tag{2.11}$$

with a reflected flux of $\hbar k|R|^2/m$. For $x > 0$, the transmitted wave has amplitude T and has a corresponding flux of:

$$j = \frac{\hbar k'}{m}|T|^2 \tag{2.12}$$

In quantum mechanics, the probability flux for a *real* potential, must satisfy a conservation law, that any change in the probability density is balanced by a net change in the probability flux into or out of that region,

$$\frac{\partial}{\partial t}|\psi(x,t)|^2 + \frac{\partial}{\partial t} j(x,t) = 0 \tag{2.13}$$

(which can be easily demonstrated by expanding out the first term of this equation, using the time-dependent Schrödinger equation and our definition of $j(x,t)$ in (2.11)). Since there is no time dependence in our problem (2.10), this conservation law implies that $j(x)$ must be x independent too, and thus the probability flux must be conserved

across the potential boundary,

$$\frac{\hbar k}{m}\left(1-|R|^2\right)=\frac{\hbar k'}{m}|T|^2 \tag{2.14}$$

Similarly the continuity of the wave-function and its first derivative at $x=0$ gives:

$$1+R=T \tag{2.15}$$

$$ik(1-R)=ik'T, \tag{2.16}$$

which can be solved to give the following expressions for the reflected and transmitted amplitudes, and their flux,

$$R=\frac{k-k'}{k+k'} \qquad \frac{\hbar k}{m}|R|^2=\frac{\hbar k}{m}\left(\frac{k-k'}{k+k'}\right)^2 \tag{2.17}$$

$$T=\frac{2k}{k+k'} \qquad \frac{\hbar k'}{m}|T|^2=\frac{\hbar k}{m}\frac{4kk'}{(k+k')^2} \tag{2.18}$$

From these equations we can easily see that the conservation of particle flux (2.14) is satisfied and that there is some proportion of flux reflected from, and transmitted through the boundary. When $E \gg V$, so $k' \to k$ then the reflected flux tends towards zero, that is, the potential step hardly affects the incident particle at all and it is fully transmitted to the boundary.

When $E < V$ then k' becomes imaginary:

$$E_\perp < V \qquad k'=i\sqrt{\frac{2m}{\hbar^2}(V-E_\perp)} \tag{2.19}$$

and therefore, we find:

$$|R|^2=\left(\frac{k-k'}{k+k'}\right)\left(\frac{k-k'}{k+k'}\right)^*=1. \tag{2.20}$$

This is the condition for total reflection of the particle.

However, importantly, the transmitted amplitude does not vanish in this case:

$$T = \frac{2k}{k + i|k'|} \tag{2.21}$$

and therefore the neutron still penetrates the boundary with an exponentially decaying wave, with a characteristic penetration length $1/|k'|$.

Returning to our original aim in this section, we see that in order to contain a neutron within a material bottle, we must find a suitable material with a large enough mean Fermi-potential V_F such that neutrons of total energy E can be totally internally reflected at all angles of incidence. Indeed this relationship can be used to *define* the energy regime of ultra-cold-neutrons; by definition, ultra-cold-neutrons are those of energies low enough that they undergo total internal reflection at any angle of incidence.

2.3.1.4 Loss of UCN on reflection

In the previous section we have seen how to describe the reflection of UCN from material boundaries and we found that the energy regime of UCN is defined as that which can be reflected from all angles and thus stored. There are however other processes involved in the UCN-boundary interaction that complicate this picture, and limits the total time we could theoretically expect to store UCN for in a material bottle (the theoretical maximum being the UCN beta-decay lifetime mentioned in section 2.3.2). The two processes discussed in this section are neutron absorption by nuclei on the material boundary, and inelastic up-scattering (i.e: scattering where the final neutron energy is higher than the initial value, and in the case of UCN this is usually

greater than the potential barrier of the material).

As shown in (2.21), even in the case of total reflection of the neutron, the wave-function still penetrates the surface. During this time the neutron can be 'captured' by a nucleus of the material, described by the absorption cross section σ_a. The neutron can also be inelastically scattered by the continuous thermal-vibration of the material's atoms. For neutrons of such low energy as UCN, the inelastic scattering is almost entirely up-scattering in this case, with the neutron gaining so much energy from the collision that it leaves the UCN energy regime, and thus, is no longer contained by the material's Fermi potential. Thus, the cross-section for inelastic up-scattering, σ_{in} for UCN, is considered as another loss cross-section.

The Imaginary Potential, W

Since both of these interactions are effectively irreversible in this case, we can treat their effect on the incident neutron as a though it was produced by an effective imaginary potential. An imaginary potential, $-iW$, in the Schrödinger equation causes the probability density to decay exponentially.

We can see this by considering a complex potential, $U = V - iW$, and try to derive an analogous conservation law to that for a real potential as in (2.13). Consider the rate of change of the probability density,

$$\frac{\partial}{\partial t}|\psi(x,t)|^2 = \frac{\partial \psi^*}{\partial t}\psi + \psi^*\frac{\partial \psi}{\partial t} \tag{2.22}$$

and using the Schrödinger equation and its complex conjugate,

$$i\hbar\frac{\partial \psi}{\partial t} = -\frac{\hbar^2}{2m}\frac{\partial^2 \psi}{\partial^2 t} + U\psi \tag{2.23}$$

$$-i\hbar\frac{\partial \psi^*}{\partial t} = -\frac{\hbar^2}{2m}\frac{\partial^2 \psi^*}{\partial^2 t} + U^*\psi^* \tag{2.24}$$

we can substitute to find,

$$\frac{\partial}{\partial t}|\psi(x,t)|^2 = \frac{1}{i\hbar}\left(-\frac{\hbar^2}{2m}\left(\psi^*\frac{\partial\psi}{\partial t} - \frac{\partial\psi^*}{\partial t}\psi\right) + (U-U^*)\,\psi\psi^*\right) \quad (2.25)$$

$$= -\frac{\partial}{\partial t}j(x,t) + \left(\frac{U-U^*}{i\hbar}\right)|\psi|^2. \quad (2.26)$$

If U is real, then we get the same equation as before (2.13), but for a complex potential $U = V - iW$, then $U - U^* = -2iW$ and thus we get a new conservation equation:

$$\frac{\partial}{\partial t}P(x,t) + \frac{\partial}{\partial t}j(x,t) + \frac{2W}{\hbar}P(x,t) = 0, \quad (2.27)$$

where $P(x,t) = |\psi(x,t)|^2$ and the third term represents the additional rate of loss of probability density due to the imaginary potential W:

$$\delta\left(\frac{\partial P(x,t)}{\partial t}\right) = -\frac{2W}{\hbar}P(x,t) \quad (2.28)$$

$$\Rightarrow \qquad P(x,t) = P(x,0)e^{-2Wt/\hbar}. \quad (2.29)$$

The Loss Cross-section

Having determined that we can represent the irreversible loss-interactions of UCN and our material through the introduction of an imaginary potential W, we need to provide a description of this potential that applies to the interactions we are interested in: UCN absorption by nuclei, and inelastic up-scattering from thermal vibrations.

The neutron absorption interaction cross-section, σ_a, grows as the velocity v of the neutron decreases:

$$\sigma_a \propto 1/k \propto 1/v. \quad (2.30)$$

This relation holds in the case where the interaction responsible for the absorption (the nuclear strong force) is confined to a region which is

much smaller than the neutron wavelength and decreases outside this region [7]. This relation essentially follows from the definition of the cross-section itself as the number of events per unit time divided by the incident flux density; it depends on the time the incident neutron spends in the vicinity of the nucleus.

For low enough incident neutron energies, the inelastic scattering cross-section, σ_{in} satisfies (2.30) [7]. Therefore, we can define a total 'loss' cross-section:

$$\sigma_l \equiv \sigma_a + \sigma_{in}. \tag{2.31}$$

as the sum of the absorption and inelastic scattering cross-sections. Experiments measuring the transmission of cold-neutrons through homogenous substances are presented in many publications and in all cases confirm the $1/v$ law for the total absorption and inelastic scattering cross-sections [8].

Probability of Loss Upon Reflection

We can then obtain a correct description of neutron loss at the boundary by setting [6],

$$W = \frac{\hbar}{2} \sum_i N_i \sigma_a^i v \tag{2.32}$$

$$\Rightarrow \qquad 1/\tau_{abs} \equiv 2W/\hbar = \sum_i N_i \sigma_l^i v, \tag{2.33}$$

where the index i, represents a sum of the nuclear species present in the material, N_i is the density of that species, and τ_{abs} represents the effective absorption decay-lifetime. Essentially the same result is obtained from the the rigorous calculation of Goldberger and Seitz [9]. Note that W is independent of neutron velocity.

Substituting (2.33) into our definition of the complex potential $U =$

Element	$a_{\text{coh}}^{\text{bound}} \times 10^{-13}$cm	σ_{tot} (barns)	V_F (neV)	$f = W/V \ \times 10^{-5}$
Be	7.75	0.22	252	0.08
Ni	10.6	48	252	12.5
Fe	7.9	8.5	210	8.5
C	6.6	1.4	180	0.6
Cu	7.6	43.5	168	15.5
Al	3.45	2.8	54	2.25

Table 2.1: Common fermi potentials [6]

$V - iW$ and comparing with (2.9), we have,

$$U \equiv V - iW = \frac{2\pi\hbar^2}{m} N(b - ib_l), \tag{2.34}$$

where,

$$b_l = \left(\frac{\sigma_l k}{4\pi}\right) \tag{2.35}$$

From this we can calculate the ratio W/V, which we shall denote as the loss-factor, f,

$$f \equiv \frac{W}{V} = \frac{\sigma_l k}{4\pi b} = \frac{\sigma_l}{2b\lambda} \tag{2.36}$$

Comprehensive lists of values for the neutron scattering lengths and loss cross-sections for various materials (eg: the ILL Data Book, [10]) can be used to calculate f, and a useful table of relevant materials is produced in Golub (1991) [6]. A couple of interesting values are reproduced in table 2.1.

With the equation for U (2.34), we can return to our expression for the reflection coefficient (2.18), replacing V with U,

$$|R|^2 = \left|\frac{k - k'}{k + k'}\right|^2 = \left|\frac{\sqrt{E} - \sqrt{E - U}}{\sqrt{E} + \sqrt{E - U}}\right|^2 \tag{2.37}$$

which can be expanded out to (see [6]),

$$|R|^2 = \frac{E - \sqrt{E}\left[2\alpha - 2(V-E)\right]^{1/2} + \alpha}{E + \sqrt{E}\left[2\alpha - 2(V-E)\right]^{1/2} + \alpha} \tag{2.38}$$

where,

$$\alpha = \sqrt{(V-E)^2 + W^2} \tag{2.39}$$

This gives a complete expression for the *probability of reflection per bounce*.

When $W \ll V \;\Rightarrow\; f \ll 1$, which is usually the case for materials typically used for UCN storage (as in table 2.1), we can expand the square roots in (2.38) and keep only terms to first-order in W,

$$|R|^2 = 1 - 2f\left(\frac{E}{V-E}\right)^{1/2} \equiv 1 - \mu(E) \tag{2.40}$$

where we have introduced the quantity $\mu(E)$ which represents the *probability of loss per bounce*. Note that throughout this section we have treated the problem in one-dimension, where E is the transverse energy, perpendicular to the boundary. Rewriting this in terms of the total energy and the angle of incidence relative to the surface normal, $E_\perp = E\cos^2\theta$ we get,

$$\mu(E,\theta) = 2f\left(\frac{E\cos^2\theta}{V - E\cos^2\theta}\right)^{1/2} \tag{2.41}$$

The expressions for the probability of reflection in (2.38), and in the simplified case of $f \ll 1$, the probability of loss in (2.41) provide a first-order description of the neutron-material interaction. Further considerations for a complete description of the interaction include more complicated surfaces than a simple, idealistic potential step, such as multi-layered surfaces, or rough surfaces, all of which have an impact on the reflection probability.

2.3.2 Neutron Beta Decay; The Weak Interaction

From the preceding discussion of the interaction of UCN with material boundaries, we concluded that UCN of energy E that is lower than the Fermi potential of the material V_F undergo total reflection at all angles of incidence, and thus can be stored until they are either absorbed upon reflection by nuclei in the material, or are scattered by the atom's thermal vibrations to an energy much greater than V_F. By carefully choosing a material for a neutron storage cell that has a very low loss-factor f (2.36) we can increase the effective time we can store UCN. However, the free neutron isn't itself stable and undergoes β^- decay, due to the effect of the weak interaction, which forms an effective hard upper limit on the maximum time a density of neutrons can be contained for.

In β^- decay, the neutron is converted into a proton while emitting an electron and an electron anti-neutrino,

$$n = p + e^- + \bar{\nu}_e \tag{2.42}$$

with a mean-lifetime of $\tau_\beta = 885.7 \pm 0.8\,\mathrm{s}$ [11]. This implies that, the maximum time we could hope to keep a meaningful density of UCN for would be of order $\sim 10^3$ seconds.

2.3.3 The Gravitational Interaction

The gravitational potential due to the earth's gravitational field is given by,

$$V_g = m_n g h \;\approx 102 \times 10^{-9}\,\mathrm{eV\,m^{-1}} \tag{2.43}$$

From table 2.1, we can see that even for materials with some of the highest fermi-potentials, such as Beryllium $V = 252$ neV, the gravitational potential energy change over a vertical height of just 1m is

a significant fraction of the neutrons' kinetic energies. This places a restriction on arrangement of neutron guides in experiments that wish to retain the absolute maximum density at all times as significant vertical drops will shift the velocity spectrum and lead to more losses through boundary collisions, however it can also be useful for improving the UCN transmission probability through detector windows or polarising foils.

2.3.4 Magnetic Dipole Moment

The neutron possesses a magnetic dipole moment $\mu_n = -1.913\mu_N$, where $\mu_N = e\hbar/2m_p$ is the nuclear magneton, arising from its charged quark constituents. The existence of this anomalous magnetic moment provided some of the first evidence that the neutron is a composite particle. The potential energy V of a neutron in a magnetic field $\vec{B}$, is given by the interaction of the magnetic dipole moment $\vec{mu}$, which is aligned along the axis of spin, as follows,

$$V = -\vec{\mu} \cdot \vec{B} \tag{2.44}$$

When we are considering UCN in the presence of magnetic materials we must add this potential to the Fermi pseudo potential 2.9,

$$V = \frac{2\pi\hbar^2}{m} \sum_i N_i b_i \mp \mu B \tag{2.45}$$

where the choice of sign is determined by the orientation of the neutron spin relative to the magnetic field. For ferromagnetic materials, these two terms can be of comparable magnitude, so the probability of a UCN being reflected by a magnetic surface depends on the orientation of the neutron spin relative to the magnetic field. This can be utilised to polarise UCN by using a magnetised foil to preferentially reflect one spin state and allowing the other to be transmitted.

2.4 Principles of the Experiment

Like any other body with a magnetic moment the neutron can therefore be made to precess in a magnetic field about an axis parallel to the field. Being a spin-1/2 particle it has the possibility of having its magnetic moment vector aligned or anti-aligned with the spin. The energy associated with this precession adds to the Hamiltonian the term $-\vec{\mu_n} \cdot \vec{B}$. Thus these two $M_J = \pm 1/2$ energy levels are separated by $\Delta E = 2\vec{\mu_n} \cdot \vec{B}$ with an associated Larmour precession frequency $\nu = \Delta E/h = 2\vec{\mu_n} \cdot \vec{B}/h$.

If the neutron also possesses an electric dipole moment d_n and is subject to an electric field then this will provide additional torque to the precession and correspondingly add to the Hamiltonian in a similar fashion. If both $\vec{E}$ and $\vec{B}$ fields are present and parallel then the Hamiltonian is,

$$H = -2(\vec{\mu_n} \cdot \vec{B} + \vec{d_n} \cdot \vec{E}) \quad (2.46)$$

$$= -2\vec{s} \cdot (\mu_n \vec{B} + d_n \vec{E}) \quad (2.47)$$

If the electric field is anti-parallel relative to the B-field then the hamiltonian is,

$$H = -2\vec{s} \cdot (\mu_n \vec{B} - d_n \vec{E}) \quad (2.48)$$

The energy difference between parallel and anti-parallel fields is then $\Delta E = 4\vec{d_n} \cdot \vec{E}$ with a corresponding shift in precession frequency of,

$$\Delta\nu = 4\vec{d_n} \cdot \vec{E}/h \quad (2.49)$$

Thus the principle of the experiment is to measure as accurately as possible the difference in precession frequency between parallel and anti-parallel electric and magnetic fields.

2.4.1 Ramsey Method of Separated Oscillating Magnetic Fields

An electric dipole moment of $10^{-27}\, e \cdot \mathrm{cm}$ in a $10\,\mathrm{kV/cm}$ electric field would produce a frequency shift of just $0.01\,\mu\mathrm{Hz}$. To measure such small differences in frequency, Norman Ramsey devised an experiment that could accurately determine the precession frequency of molecules in a beam. The molecules in his experiment passed through two regions of phase-coherent oscillating magnetic field during their flight. In the Cryo-EDM experiment a similar technique is used however the neutrons are trapped in a bottle and the oscillating pulses are seperated in time not in space.

The neutrons are spin polarized before entering the apparatus and stored in a moderate magnetic field B_{0z}, approximately $5\mu T$, defining their spin and making them precess about the field's principle axis (z). The neutrons are then subjected to an oscillating magnetic field B_{xy} perpendicular to the static B_{0z} field with a frequency close to that of the neutron's precession. The duration and amplitude of B_{xy} is arranged so that this pulse rotates the spin vector of the neutrons down to the xy-plane, perpendicular to the original B_{0z} (and it is thus known as the $\pi/2$ pulse). The oscillating field is then shut off and the neutrons are allowed to precess in this plane for a time T_s much longer than the oscillating pulse.

After T_s, the ocillating field B_{xy} is then switched on again (phase coherent with the first pulse). If the oscillating field had a frequency that exactly matched that of the neutrons' precession frequency then this pulse would simply continue to rotate the spin a further $\pi/2$ down along the $-z$ axis so that all the neutrons would end up in the opposite spin state from the initial one.

However if the frequency of precession of the neutrons' spin vectors and the oscillating field were slightly different than during the free

precession between pulses, a phase difference would build up between the two. The result of the second $\pi/2$ pulse is a function of this phase difference - as it varies away from zero there is a probability that the second pulse will rotate the neutron spin back up instead of continuing to rotate it down. Figure 2.2 shows this graphically,

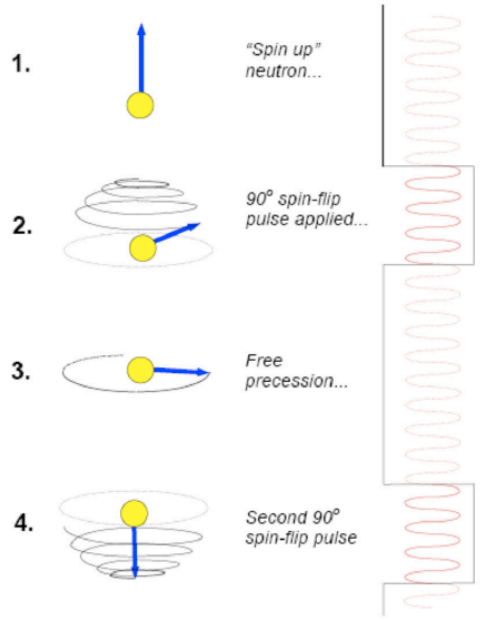

Figure 2.2: Schematic diagram of the Ramsey resonance technique [4].

After this the neutrons are collected and their spin state is analysed on detection and the ratio of neutrons having spin up to spin down relates directly to the phase difference that has build up over the storage time. Near the resonant frequency, the relation between the frequency difference and the neutron count is given by,

$$N_{\uparrow\downarrow}(\nu) = \bar{N_{\uparrow\downarrow}} \mp \alpha_{\uparrow\downarrow} \bar{N_{\uparrow\downarrow}} \cos\left(\frac{\pi(\nu - \nu_0)}{\Delta\nu}\right) \tag{2.50}$$

where $\bar{N}$ is the average number of neutrons in the spin state $\uparrow$ or $\downarrow$ and ν_0 is the neutron resonant frequency. An example of this curve is shown in figure 2.3. α is given by,

$$\alpha = \frac{N_1 - N_2}{N_1 + N_2} \tag{2.51}$$

where N_1 and N_2 are the maximum and minimum counts on the Ramsey curve. $\Delta\nu$ defines the linewidth, which is the distance between a maximum and minimum, and can be written in terms of t, the duration of the oscillating magnetic field pulses, and T_s, the free precession time of the neutrons between the two pulses,

$$\Delta\nu = \frac{1}{2(T_s + 4t/\pi} \approx \frac{1}{2T_s} \quad \text{for} \quad 4t/\pi << T_s \tag{2.52}$$

Thus for detecting a potential electric dipole moment of the neutron, we apply a large E-field during a long period of free precession time T_s to cause a detectable frequency shift, due to the neutron EDM's interaction with the electric field. During this period an additional phase difference will build up between the neutrons and the oscillating magnetic field, thus after the second pulse there should be a difference in the number of neutrons counted in a particular spin state relative to the expected Ramsey curve.

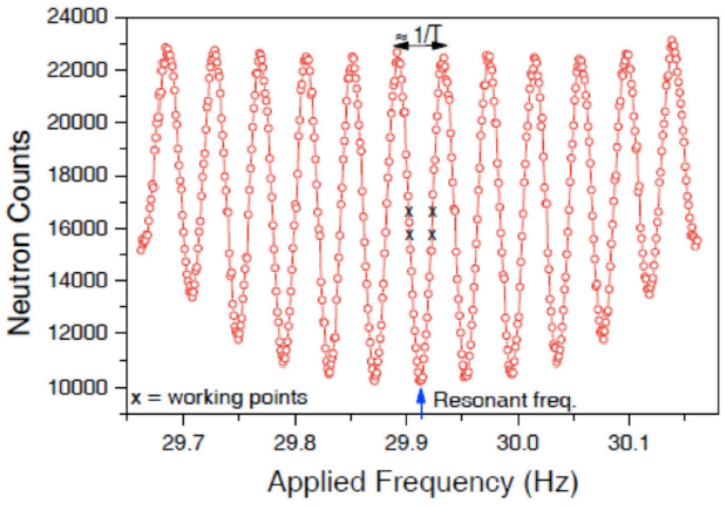

Figure 2.3: Example of a resonance curve [4].

CryoEDM statistical uncertainty

The statistical uncertainty on the EDM measurement can be shown to be,

$$\sigma_{d_n} = \frac{\hbar}{2\alpha E T_s \sqrt{N}} \tag{2.53}$$

where N is the total number of neutrons detected. Note that the uncertainty in the frequency is inversly proportional to the time of free precession of the neutons in between the pulses. Thus to minimise the uncertainty, the experiments needs a good visibility of the Ramsey fringes, so a good level of polarisation of the neutrons and $\alpha \approx 1$, a long period of free precession T_s, a large number of neutrons N and a strong electric field E.

2.5 CryoEDM Overview

To close this chapter we include a brief overview of the design of the CryoEDM apparatus.

One of the advantages of a cryogenic neutron EDM experiment compared to earlier room temperature based experiments is the potential to obtain larger densities of neutrons in the measurement cell. In 1975, Golub and Pendlebury [12] proposed a technique for obtaining UCN densities an order of magnitude higher than those obtained from neutrons at thermal equilibrium with a moderator. The technique has been termed 'Superthermal UCN production' and involves the down-scattering of cold neutrons with wavelength of $\lambda = 8.9$Å by superfluid ^{4}He at 0.5kelvin to convert them to UCN.

Golub and Pendlebury note three further features of ^{4}He which make it ideal as a medium for UCN; it has zero neutron absorption cross section; it's critical energy for total internal reflection is about 10 times

smaller than that of most of the common wall materials; neutrons are scattered by ^{4}He in a purley coherent manner preserving their initial polarisation.

Another advantage of the cryogenic environment is in the area of magnetometry, which is one of the main challenges in any EDM measurement. One of the main systematic errors in the room temperature experiment was the geometric-phase induced false EDM effect [13] from the cohabiting mercury magnetometer. The cryogenic experiment will use SQUIDs to measure the magnetic field, which operate at low temperatures in superfluid helium avoiding this systematic error.

Figure 2.4 shows an cutaway through the side of the experiment.

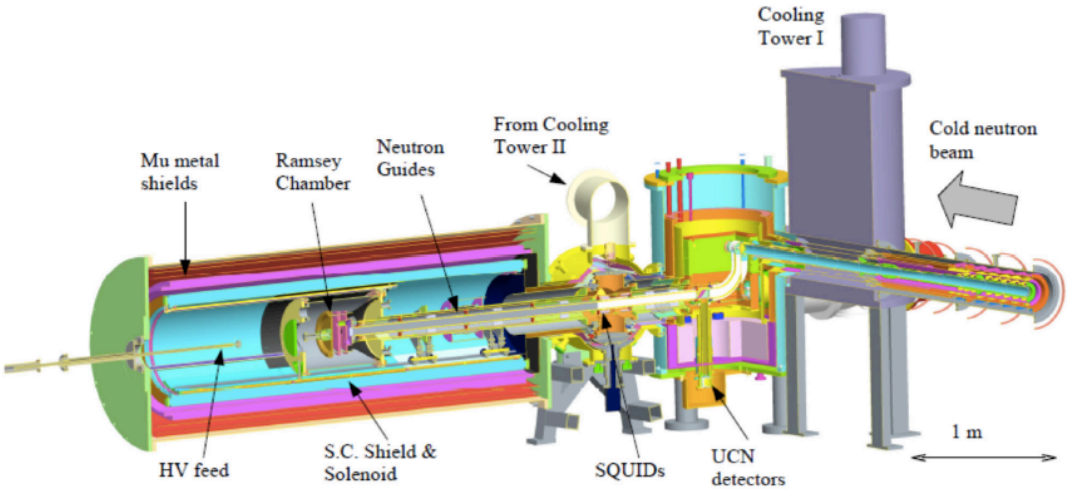

Figure 2.4: An overview of the cryoEDM experiment [14].

Starting from right to left on this diagram the major features of the experiment are:

- The ultra-cold neutron production volume, consisting of a 2m long cylindrical volume filled with superfluid helium that converts polarized cold neutrons from the reactor into ultra-cold neutrons.

Surrounding this tube are magnetic coils are shielding to retain the neutrons' polarisation.

- The UCN guide tubes down into the measurement cell. This consists of a long section of UCN guide tubes that drop down away from the source and turn 90degrees into the magnetic shielded region where the Ramsey cell is situated. The drop of roughly 30cm from the source region to the measurement region ensures that the neutrons within the measurement cell are able to fill the complete available phase-space in this region.

- The Ramsey cell. At the end of the guide tubes and situtated centrally inside the layers of magnetic and thermal shielding, is the Ramsey cell, which consists of two chambers - one with a high-voltage electrode and the other without, allowing each run of the apparatus to carry out two experiments, one with and one without an electric field.

- After the Ramsey technique has been applied, the neutrons are then emptied out of the Ramsey cell and head back down the UCN guide tubes down to the detector region near to the UCN source, which at this point will be opened to the UCN allowing them to be detected and their spins analysed.

3 The Design of the Simulation

This chapter describes some of the key design decisions of the simulation and the important details about the way it was implemented. The chapter ends with a short summary of some tests carried out of the simulation under specific geometries that can be compared to theoretical models.

3.1 Design Overview

The simulation is written in the C++ programming language and is based around the ROOT C++ framework [1] that is very popular in high-energy physics for data analysis and simulations.

The scope of the simulation is as follows:

- Ultra-cold neutrons move under gravity through 3D geometries that can be arbitrarily complex
- Geometries can be composed from the intersection, union and subtraction of individual volumes made out of cylinders and cuboids
- The interaction of UCN with the wall material is simulated with monte-carlo methods, and the cross-sections for inelastic-scattering and absorbtion of the neutron by the wall material can be input for each volume in the geometry individually.

[1] `https://root.cern.ch`

- The neutrons will beta-decay according to a probability distribution based on the neutron beta-decay lifetime.

- A field map can be given to the simulation consisting of an arbitrary map of field vectors in 3D space. It assumes no structure (grid, cylindrical or otherwise) to the points and uses a 3-D binary-tree data-structure to store these points along with an implementation of a N-nearest neighbour algorithm to facilitate looking up the field at arbitrary points along a particle's trajectory.

- The neutrons have a spin and this interacts with a magnetic field map to correctly track the spin propagation according to the quantum mechanics.

- The interaction of the neutron spin with an electric field has been implemented but not fully tested so it will not be discussed in this thesis.

The decision to use ROOT as the primary framework was because it offered a basic geometry package that provided 3D visualisations and some useful mathematical libraries for polynomial solving.

The following sections go into more depth on the design of the key components mentioned above.

3.2 Particle Model

The particle is naturally one of the central classes in the whole simulation and contains a large portion of the critical physics algorithms. To try to limit the size of this one class, certain aspects of the particle have been broken out into sub-classes to try to better encapsulate the various physics processes that we are simulating.

3.2.1 Particle Attributes

Internally a particle is defined by the following:

- A unique ID number, labelling the particle in the full set of particles to be simulated
- A time, tracking the simulated time as the particle evolves
- A position 3-vector
- A velocity 3-vector
- A state object [see below], reflecting one of various pre-defined simulation 'states' a particle can be in.
- A spinor object, reflecting the components of the particles spin doublet as it interacts with any potential electromagnetic fields.
- The state of the pseudo random number generator at the time the particle was created

The time tracks the 'lab' time of the simulation, so that a particle that is defined as being 'created' (that is, produced in the neutron source) at a time later than the beginning of the simulation (always defined as the zero time) would have it's initial time set to this same non-zero value. So a particle's time coordinate does not measure the time since a particle was created. This actually makes it easier to monitor and compare the states of various particles and only really has implications for the implementation of the beta-decay process, since this calculation uses the time since a particle was created, rather than the lab-time.

3.2.2 Particle State

The particle state object is an implementation of the 'State' programming design pattern [2] and is used as a way of enabling the particle to behave differently depending on the type of state it is in so a particle that has been detected or absorbed no longer responds in the same way as a particle that is still propagating.

The particle states defined are,

- Propagating, the initial state of the particle and the only 'active' state in which a particle is moving through the simulation
- Detected, the state when a particle is absorbed by a detector
- Absorbed, the state when a particle is absorbed or otherwise upscattered and 'lost' through an interaction with the material walls of the neutron guides/bottle.
- Decayed, the state when a particle undergoes beta-decay
- Lost, a debugging state, to signify a particle has reached a section of the geometry that it should not be possible to reach.
- Anomalous, another debugging state, to signify the particle has undergone a transition (step, bounce or otherwise) that has left it in an inconsistent condition, as expected by the routine.

The interfaces of the classes are all the same but their response to the various methods are very different with only the progating state actually moving the particle through the geometry. The propagating class therefore contains the bulk of the algorithms governing how the

[2] `https://en.wikipedia.org/wiki/State_pattern`, see `https://en.wikipedia.org/wiki/Design_Patterns:_Elements_of_Reusable_Object-Oriented_Software` for more details.

particle moves through the simulation.

3.3 Particle Motion Under Gravity

This section provides an overview of how the simulation calculates particle motion under gravity through a 3D geometry. We will first discuss the theoretical calculation and then we will discuss a few of the particular implementation challenges that were faced.

Overview of the theoretical calculation

The physics of UCN moving under gravity is that of classical projectile motion. For UCN within a guide tube, this calculation is essentially one of finding the next point of intersection of the neutron's trajectory with the boundary of the material container it is within. We then perform a calculation at that point to determine whether any state change (absorbtion, decay, inelastic scattering) of the neutron takes place and if not, then we reflect the particle (either specular or diffuse reflection) and start the whole process again.

The ROOT framework contains algorithms to find these intersections points, however they do not cover the motion of particles under gravity, therefore we have had to implement our own solution to calculate these paths.

In early implementations of this we initially used a process of taking small steps along a straight line, and then correcting our final position due to gravity. The advantage of this approach is that there are ready made algorithms for finding the intesection of a straight line with any plane (the plane being the material wall) and therefore the implementation is simpler.

We found however that this introduces problems when you move close to the boundary and these small corrections come to determine whether you hit the boundary or not – or even whether you intesect with one boundary or another. Therefore this approach needs to be done incredibly carefully and the size of the small steps must be adjusted continually as a particle moves to account for these problems.

It was decided therefore that it would be simpler to actually do the full calculation of finding the intesection of a parabola with the boundary. As we will show shortly, this calculation is essentially one of solving for the roots of a polynomial of degree determined by the shape of the boundary. This has has it's own disadvatages however in that this calculation cannot be solved analytically for shapes more complicated than a cuboid, cylinder or sphere. However we found that this limitation was not as significant for the kinds of geometries we wished to build for simulating the CryoEDM apparatus, as we can construct geometries of arbitrary complexity by taking mixing these basic shapes together.

Thus the method used for calculating the particle's motion is one of 'parabolic ray-tracing'.

Parabolic Ray-Tracing: an example calculation for a flat Plane

This section runs through an example calculation of a parabola with a flat plane to illustrate the process of how the simulation calculates particle motion. The calculation for other shapes such as the cylinder are discussed at the end and are a slight modification to this idea.

To begin with we will run through the basic calculations involved in performing a single ray-tracing-like 'step' of a particle under gravity. Consider a particle with a position vector $X_i(t_0) = (x(t_0), y(t_0), z(t_0))$ that is within a coordinate system that is defined by some master

volume that we typically refer to as the world or global frame. Now consider the same particle that is now enclosed within another volume that is rotated with respect to the global frame, figure 3.1

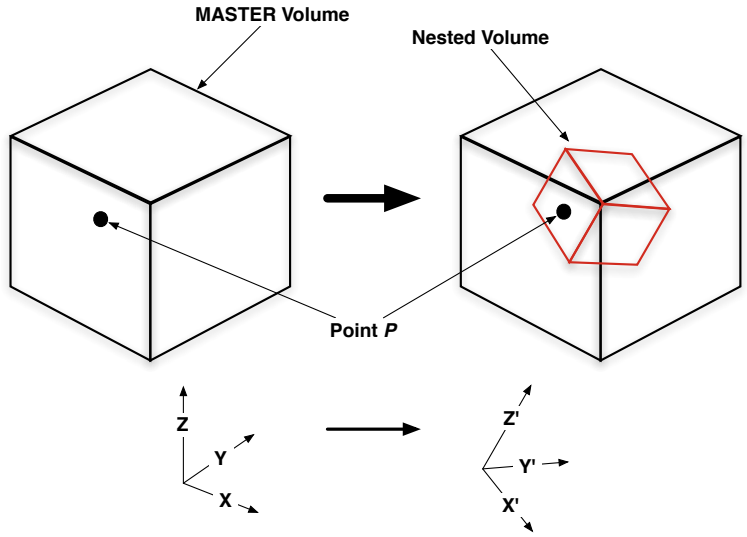

Figure 3.1: A simple geometry hierarchy of a single box, rotated with respect to the global volume.

where the particle at point P, transformed into the 'local' coordinate frame of the rotated box, is given by $X_i'(t_0) = (x'(t_0), y'(t_0), z'(t_0)) = M_{ij}X_j$, and where M_{ij} is some transformation matrix representing the rotation of the box.

Whenever we perform a calculation we will always work in the local coordinate frame of the volume that the point is contained by. Then once we have found the intersection point of the next boundary in the local frame, we transform our point back to the global coordinate system and do the actual propagation there.

Our particle has an initial momentum, $P_i(t_0)$, which in the local frame is given as above by $P_i'(t_0)$. It is clear that, as long as the particle has a non-zero momentum that there will always be exactly two intersections with the boundaries of the box (ie: an entry point and an exit point), as depicted in figure 3.2.

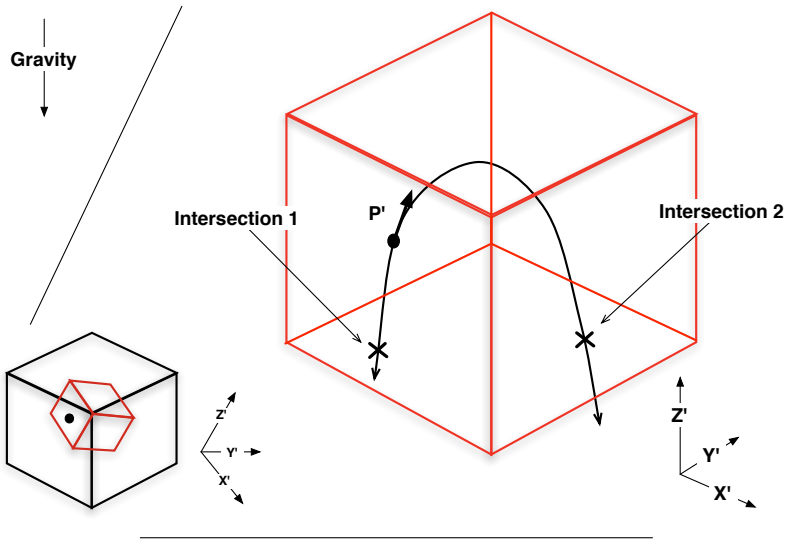

Figure 3.2: An example of a single track inside the box, viewed from the local coordinate frame of the box. There will always be at least two intersections with the boundaries of the box

The aim of a parabolic tracking routine is to calculate these intersection points. To do this, we must consider each boundary in turn, so for the box that means we consider each side of the box as a separate plane, and determine if and where there is an intersection. So for example, consider that we are working in the local coordinate frame of the box, and we have a single non-zero component of the momentum, say $p'_x(t_0) \neq 0$, and a single corresponding boundary of the box, for example, the positive-X boundary $x'(t) = +L, -\infty < y'(t) < +\infty, -\infty < z'(t) < +\infty$.

Using the standard equation for gravitational motion, we can solve the x-component

$$X_i(t) = X_i(0) + \dot{X}_i(0)t + \frac{1}{2}g\hat{G}_i t^2 \qquad \text{where, } i = 1, 2, 3 \qquad (3.1)$$

where, $X_i(t)$ is the position vector of the particle at a time t, g is the gravitational free-fall acceleration of a particle and where $\hat{G}_i$ is a unit vector signifying the direction of the earth's gravitational field - usually pointing straight down along the z-axis by convention. We can

solve the x-component equation to find the time of intersection with the $x'(t) = +L$ plane.

$$
\begin{aligned}
x'(t) = +L &= x(0) + \dot{x}'(0)t + \frac{1}{2}g\hat{G}_{x'}t^2 && (3.2)\\
\Rightarrow \quad 0 &= (x'(0) - L) + \dot{x}'(0)t + \frac{1}{2}g\hat{G}_{x'}t^2 && (3.3)\\
\Rightarrow \quad 0 &= at^2 + bt + c && (3.4)
\end{aligned}
$$

which is a quadratic equation for t. This equation gives all possible intersections with the entire $x'(t) = +L$ plane as depicted in figure 3.3; two solutions represent a particle that crosses the boundary twice, one solution means one intersection and so on. A negative solution means the parabola intersects the boundary but only in the past when t is extended back to $-\infty$.

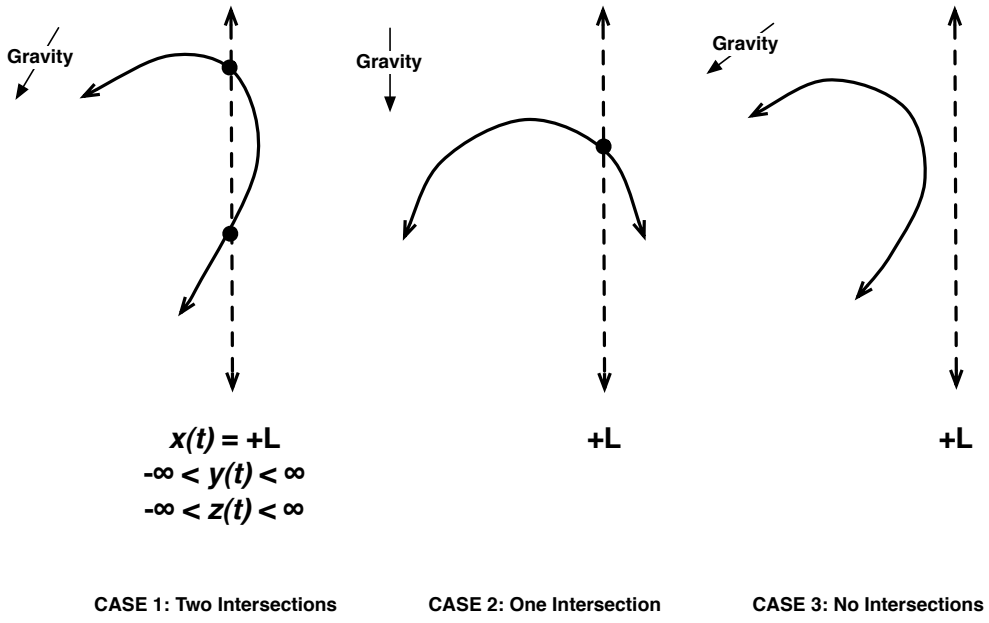

Figure 3.3: An example of a one-dimensional parabola crossing a single plane/line.

So if our particle starts inside the box, and therefore must intersect one of the boundaries along its trajectory, we must solve the equation shown above for each of the six boundaries of the box $\pm X, \pm Y, \pm Z$

and then find the **smallest**, **positive**, **non-zero** value of t from the possible solutions, which represents the intersection point with the boundary.

Calculate Distance Travelled Along Parabola

Now that we have found the time, t_1, of intersection of the particle's trajectory with the nearest boundary, we can safely make a 'step' and move our particle to this point. We then need to calculate the distance travelled in this step which can be accomplished as follows:

Consider an element of path length,

$$ds = \sqrt{dx^2 + dy^2 + dz^2} \tag{3.5}$$

Hence, the arc length of a curve is given by,

$$L = \int_{curve} ds \tag{3.6}$$

Substituting and rearranging,

$$\begin{aligned} L &= \int_{t_0}^{t_1} dt \sqrt{\left(\frac{dx}{dt}\right)^2 + \left(\frac{dy}{dt}\right)^2 + \left(\frac{dz}{dt}\right)^2} \\ &= \int_{t_0}^{t_1} dt \sqrt{\left(v_x(0) + g\hat{G}_x t\right)^2 + \left(v_y(0) + g\hat{G}_y t\right)^2 + \left(v_z(0) + g\hat{G}_z t\right)^2} \\ &= \int_{t_0}^{t_1} dt \sqrt{|v(0)|^2 + 2g\left(v_x(0)\hat{G}_x + v_y(0)\hat{G}_y + v_z(0)\hat{G}_z\right)t + g^2t^2} \end{aligned}$$

which is of the form,

$$L = \int dt \sqrt{at^2 + bt + c} \tag{3.7}$$

and can be solved by parts or looked up in integral tables,

$$L = \frac{(2at+b)\sqrt{at^2+bt+c}}{4a} + \frac{(4ac-b^2)}{8a\sqrt{a}} \arcsin\left[\frac{2at+b}{\sqrt{4ac-b^2}}\right] \quad (3.8)$$

Time to Boundary From Outside and Other Shapes

So above we have seen a simple calculation to find the time of intersection for a parabola and a plane, and the general result for the distance along a parabola. With these two formulae, we could put together a basic simulation for a particle in a box, by calculating the time to intersect a boundary for each of the six boundaries of the box, and taking the smallest, positive, non-zero value.

However if our particle starts from outside the box, we have an extra step to perform. This is to check that the smallest, positive, non-zero value for the time to intersect, actually corresponds to a point on the box, as demonstrated in figure 3.4

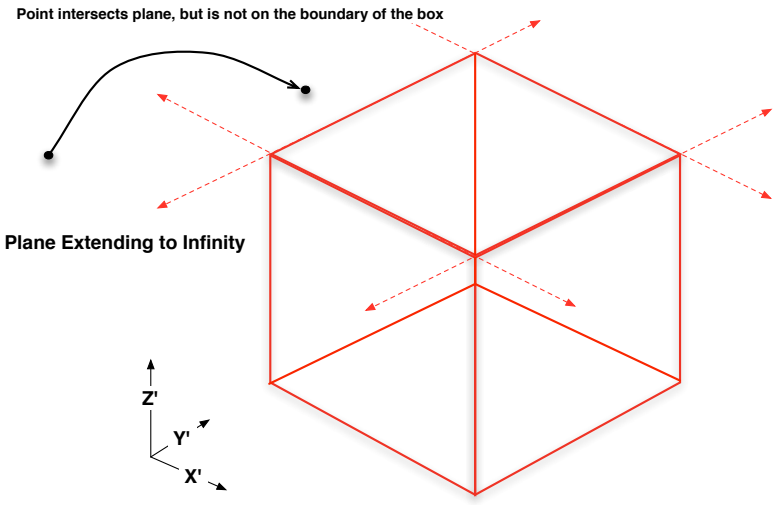

Figure 3.4: Approaching the volume from outside.

All of the above discussion applies to other shapes such as the cylinder or the torus. The only difference with these shapes is in solving the equations to find the intersections with more complicated sur-

faces. These equations are also of higher order - recall that the plane requires us to solve a quadratic, order-2 polynomial; the cylinder requires a quartic, order-4 polynomial, and the torus requires an order-8 polynomial (that cannot be solved analytically).

To show this explicitly in the case of the cylinder, consider a cylinder aligned with its horizontal dimension along the z-axis, and the circular boundary in the X-Y plane. The two ends of the tube at $z = \pm L$ can be solved for just as before, considering them as two infinite planes. The circular boundary however requires us to solve a much harder equation. The equation of a circle of radius R in the X-Y plane is, $R^2 = x^2 + y^2$. Substituting in the equations of motion of our particle under gravity gives,

$$\begin{aligned}
0 &= \Big(\frac{1}{2}g\hat{G}_x t^2 + v_x(0)t + x(0)\Big)^2 + \Big(\frac{1}{2}g\hat{G}_y t^2 + v_y(0)t + y(0)\Big)^2 - R^2 \\
&= t^4\Big(\frac{1}{2}g^2\left[\hat{G}_x^2 + \hat{G}_y^2\right]\Big) + t^3\Big(g\left[\hat{G}_x v_x(0) + \hat{G}_y v_y(0)\right]\Big) \\
&+ t^2\Big(g\left[\hat{G}_x x(0) + \hat{G}_y y(0)\right] + \left[v_x^2(0) + v_y^2(0)\right]\Big) \\
&+ t\Big(2\left[v_x(0)x(0) + v_y(0)y(0)\right]\Big) + (x^2(0) + y^2(0) - R^2) \\
&= at^4 + bt^3 + ct^2 + dt + e
\end{aligned}$$

which is the standard form of a quartic polynomial. This simply reflects the fact that there can be at most four possible intersections of a parabola and a circle, whereas there can be at most eight possible intersections between the torus and the parabola, hence the order-8 polynomial. So after solving the polynomial equation for t, we can again go through the process of finding the smallest, non-zero, positive value that corresponds to a point on the boundary.

The calculation outlined in the previous section is performed at the start of each 'Step' of the particle, where a step is each actual time the particle moves to a new location in the simulation. This calculation tells the particle the maximum distance it could move before hitting the next boundary, which it can then move to (unless a maximum step size was defined as a parameter to the simulation). However if there is a magnetic field present each of these steps will be broken down into smaller sub-steps in which the field will be measured at that point and the particle's spin will evolve under. When the particle finally hits the boundary it will calculate whether it will continue or whether it has changed state due to one of the physical loss mechanisms when interacting with a boundary, as outlined in the flow diagram in figure 3.5.

3.4 Modelling the Experiment's Geometry

Along with the particle motion algorithm discussed in the previous section, the geometry is a key part of the simulation and involved in the motion and physics of UCN-boundary interactions.

The simulation uses the ROOT framework's geometry library to provide some of the functionality such as providing the definition of shapes, materials and volumes, and providing the basic volume hierarchy, whereby there is one 'root' or 'top' volume and everything else is a sub-volume contained inside that or a descendant of this 'top'. This hierarchy is important as it enables ROOT to quickly tell you given a position, which of the volumes in the hierarchy you are within.

As mentioned in the design overview at the start of this chapter, geometries can be of arbitrary complexity by allowing the nesting of volumes within other volumes, and by making composite volumes out

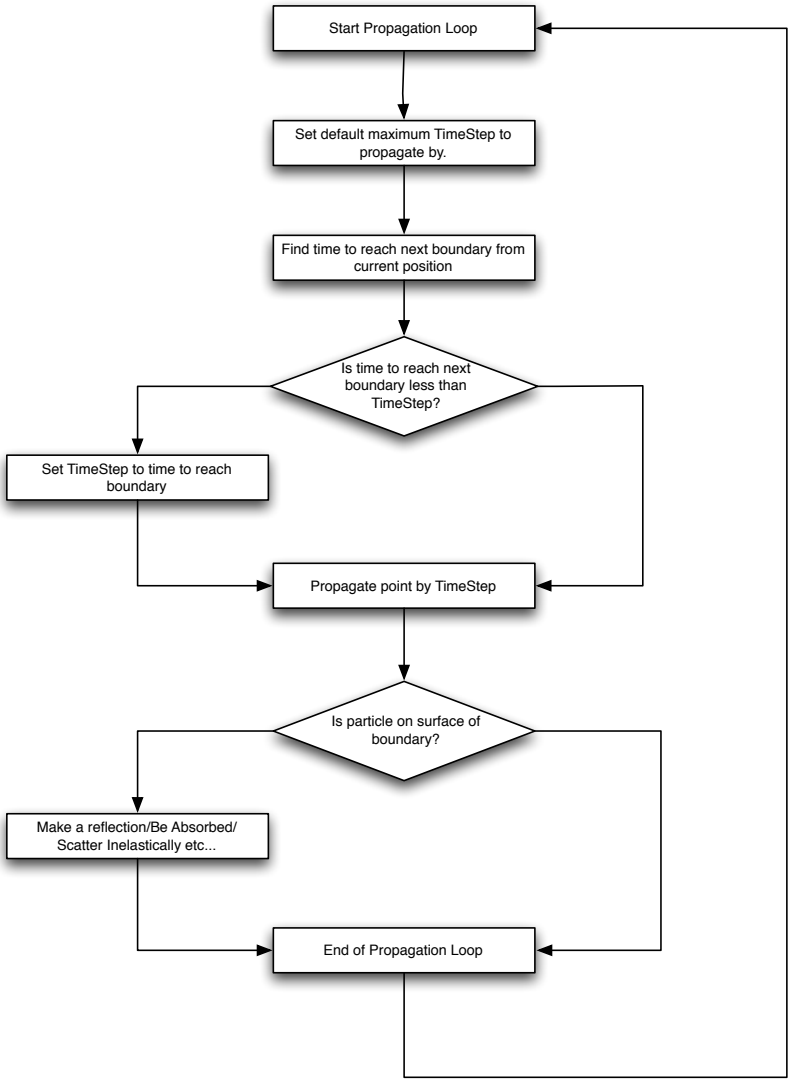

Figure 3.5: The basic decisions involved in a typical propagation loop

of the union, subtraction or intersection of volumes.

Figure 3.6, illustrates some examples of the types of volumes that can be built with ROOT.

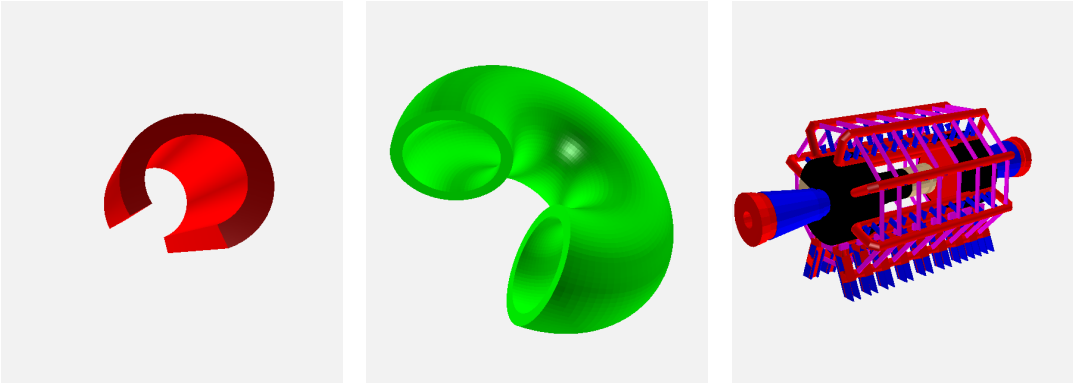

(a) A tube (b) A torus (c) Atlas Detector

Figure 3.6: Some examples of ROOT geometries

However all of this functionality has had to be largely rewritten or extended in some major ways to take into account the motion of particles under gravity as mentioned above. For example in order to provide navigation features a volume needs to be able to find the proper container of the current point of a track, which could be the volume itself, one of its daughter volumes or none if the point is actually outside the volume. Volumes also need to provide navigation methods such as computing the distance from the current point to the next boundary or which daughter volume will be crossed first. These navigational features are implemented at the shape level, and thus need to be re-implemented in the case that the motion is parabolic instead of linear.

Coordinate Systems

Calculating the motion of the particles through a 3D geometry of nested volumes requires a lot of attention paid to coordinate transformations, as each individual volume in the hierarchy has it's own trans-

formation matrix relative to the 'top' volume in the system (thought of as 'the world' or 'lab' frame). When calculating the motion of the particle within a volume, the particle's position and momentum are first translated into the volume's coordinate system to make the calculation easier, and then translated back when the intersection point has been calculated.

Materials

Every volume in the geometry has the concept of it's role and it's material. The volume's role is the concept of whether the volume serves some function, such as being a detector, or a wall, or a medium through which neutrons can pass unrestricted (eg: the interior of a container filled with liquid helium would be a volume in our geometry with the role of medium).

The material property contains the information about the neutron-material interaction cross-sections, which get calculated into Fermi-potentials and used in every neutron-boundary interaction in the simulation to determine if the neutron is to undergo a state change. These are set per-material, and each volume can have one material type.

Materials also have another property, 'roughness', that is a heuristic that functions as a way of coarsely determining the proportion of specular to diffuse reflection. A roughness of 0 would mean that every neutron reflection from a boundary would be entirely specular, whereas a roughness of 80 would mean that approximately 80% of the time the reflection will be diffuse. A diffuse reflection is one in which the particle is reflected at any angle in the half-sphere above the surface plane, with all angles having equal likelihood.

Varying Geometries

Currently the simulation expects a geometry to be loaded as an input therefore there is no support for geometries with moving volumes. One way of accomplishing this effect though is to run multiple simulations in order, so taking the output of one simulation as the input of the next with the geometry changed a little. This has only been partially tested however in the most basic case of a valve having two positions, open and closed, and there is no support for changes in neutron momentum based on the movement of a boundary.

3.5 Particle Loss or State Change

In section 3.2.2 it was discussed how each particle's state is modelled in the simulation. A particle will only propagate in the simulation's run loop when it is in the 'propagating' state, with all the other states used to track the final state of the particle.

The 'detected' state is triggered when a particle comes into contact with a 'detector'-type volume in the simulation. The detectors in the simulation are implemented in a simple manner, simply functioning as a black hole upon which, if a particle makes contact, it's state is changed to detected and it no longer propagates through the apparatus.

The neutron's interaction with the material boundaries of the experimental apparatus is tracked using the 'absorbed' state. It was mentioned in the previous section how every volume in the simulation's geometry has a material type associated, and each material has a Fermi potential defined using the material's loss cross-sections for energy up-scattering and neutron capture. At every reflection from a surface in the simulation, a calculation is performed using 2.40 to cal-

culate the probability that the neutron is scattered or absorbed, and then using a pseudo-random number generator to decide on whether this occurs on this reflection. If it does occur, the neutron is marked as in the 'absorbed' state and the propagation ends.

Neutron absorption by impurities in the liquid helium were calculated in the same manner as neutron beta-decay, by calculating a probability of decay over the period of time for each time step of the simulation, and then using the random number generator to determine if the particle decayed or was absorbed. For this reason, the volume within which the neutron's propagate also has a material defined, which is ^{4}He in this case, and also has a scattering cross-section specified which is used for this calculation.

3.6 Magnetic Fields and Spin Interactions

As stated in the previous sections, spin is a property of the particle and is calculated at multiple points along each step (how many times per step is a parameter that is input to the simulation).

Spin calculation

Particle spin evolution is calculated by storing the two-component spinor internally to the particle and calculating at every step the evolution of this spinor according to the Schrödinger equation as follows.

If we write the Hamiltonian of a general uniform static field as,

$$\hat{H} = -\gamma \left(B_x \hat{S}_x + B_y \hat{S}_y + B_z \hat{S}_z \right) \tag{3.9}$$

where $\hat{S}_i$ are the Pauli spin matrices, and if we define the angular frequencies $\omega_i = -\gamma B_i$, then we can substitue these into the Schrödinger

equation,

$$i\hbar\frac{\partial}{\partial t}|\psi(t)\rangle = \hat{H}|\psi(t)\rangle \tag{3.10}$$

along with writing the spinor as a two component vector $|\psi\rangle = \begin{pmatrix} a(t) \\ b(t) \end{pmatrix}$ to give,

$$\begin{pmatrix} \dot{a} \\ \dot{b} \end{pmatrix} = \frac{-i}{2}\begin{pmatrix} \omega_z & \omega_x - i\omega_y \\ \omega_x + i\omega_y & -\omega_z \end{pmatrix}\begin{pmatrix} a \\ b \end{pmatrix} \tag{3.11}$$

which can be solved to give,

$$a = a_0 \cos\left(\frac{\sqrt{\omega_x^2+\omega_y^2+\omega_z^2}}{2}t\right) \tag{3.12}$$

$$- \frac{i\omega_z a_0 + b_0(i\omega_x+\omega_y)}{\sqrt{\omega_x^2+\omega_y^2+\omega_z^2}} \sin\left(\frac{\sqrt{\omega_x^2+\omega_y^2+\omega_z^2}}{2}t\right) \tag{3.13}$$

$$b = b_0 \cos\left(\frac{\sqrt{\omega_x^2+\omega_y^2+\omega_z^2}}{2}t\right) \tag{3.14}$$

$$+ \frac{a_0(\omega_y - i\omega_x) + i\omega_z b_0}{\sqrt{\omega_x^2+\omega_y^2+\omega_z^2}} \sin\left(\frac{\sqrt{\omega_x^2+\omega_y^2+\omega_z^2}}{2}t\right) \tag{3.15}$$

These are the equations used by the simulation to evolve the two-components of the spinor $a(t)$ and $b(t)$. When it comes time to run an analysis on the simulation data, you can calculate the probability that the particle spin was along any axis you wish to provide in the usual manner of taking the inner product. For the probability that

the particle is along the x, y or z axes, you can use,

$$|\langle x|\psi(t)\rangle|^2 = \frac{1}{2} + \frac{1}{2}(ab^* + a^*b) \tag{3.16}$$

$$|\langle y|\psi(t)\rangle|^2 = \frac{1}{2} + \frac{1}{2}(ba^* - ab^*) \tag{3.17}$$

$$|\langle z|\psi(t)\rangle|^2 = aa^* \tag{3.18}$$

Field Maps

Fields are supported either as uniform magnetic fields with a given field strength and direction, or as field maps that are loaded from a flat file containing any arrangement of vertices with field measurements. For a field map, the collection of field measurements are read into a k-dimensional tree data structure (where in this case $k = 3$ for a 3 dimensional space), which are particularly useful for nearest neighbour searches, where given a position vector we want to find the m nearest points in the map to this position.

By not requiring the field map to take on any form, means that we can freely mix experimental data on top of a traditional grid-based lattice of field points from a magnetic field simulation say, or a theoretical calculation. Thus this solves the general case, but leaves the more optimised cases of a regular lattice field map to be implemented if required for maximum performance.

The k-d tree is a tree data structure in which every node is a k-dimensional point and in which each node has at most two child nodes usually distinguished as 'left' and 'right'. Nodes with children are parent nodes and nodes with no children are leaf nodes. There is a 'root' node too, which is the ancestor of all nodes at the top of the tree. Any node in the tree can be reached by starting at the root node and repeatedly following references to either the left or right child.

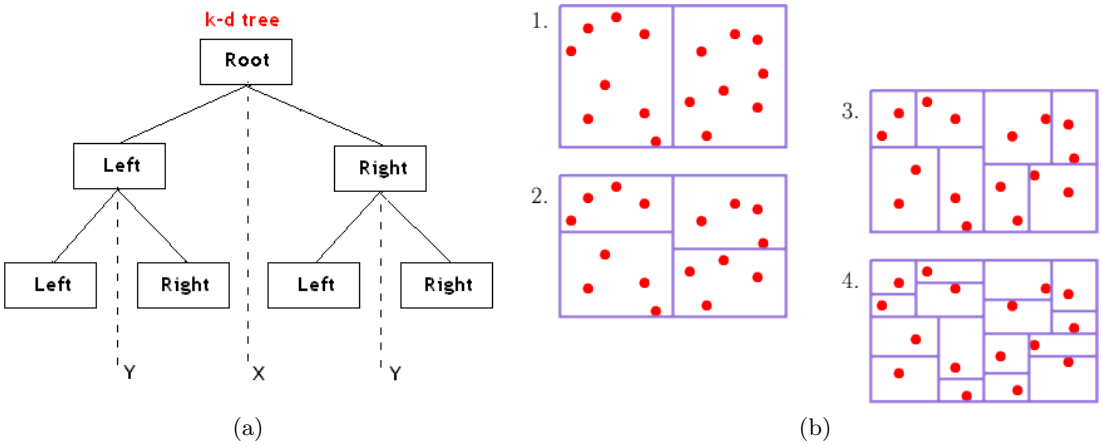

Figure 3.7: Fig 3.7a shows the start of a typical tree structure with the root node starting the splitting into two 'left' and 'right' sub-trees. For our purposes, we perform this splitting based on the x-dimension by taking the point with whose x coordinate is the median of all points as the root node. Fig 3.7b shows a 2D representation of this splitting process. Starting in 1, the points are divided up into two sub-trees, left and right. In 2 both regions split again, this time on the basis of the next dimension. In 3 these 4 regions split again, back in the original dimension and so on. Until every point is in it's own region on it's own.

Every node in the tree is associated with one of the k-dimensions, and a plane perpendicular to this dimension splits the space into two regions with points to the left of this plane falling under that node's left child and points to the right falling under the node's right child. So for example in our case of a 3-dimensional tree, if for a particular node the 'x' is chosen as the splitting axis, then all points in the subtree with x smaller than the the x coordinate of the node will appear under the left subtree and all points with larger x coordinate will appear under the right subtree. Usually the root node starts the splitting about the x coordinate and you then cycle through the axes as you move down the tree (so root's children split about y, and their children about z and so on). To ensure that the tree is 'balanced' (so that every leaf node is roughly the same distance from the root node), points are inserted by taking the median of the points being put into the subtree with respect to the axis being used to create the splitting plane, so the root node is the point whose x coordinate is the median x of all the points in the tree, and it's children are the median y of all

the remaining points and so on.

A nearest neighbour search algorithm for this tree structure has been implemented and is used when a particle in the simulation wants to find the field in its position. It starts with the particle asking the field object what the field is at its position and then the field conducts a nearest neighbour search for the n nearest points (n is configurable as a parameter) and it then finally works out the inverse-distance-weighted average of the field at these points to give the field at the particle's position.

The inverse distance weighting is calculated using the 'Modified Shepard's Method' [3] where the field is calculated using,

$$f(x) = \frac{\sum_n W_n(x) Q_n}{\sum_n W_n} \tag{3.19}$$

where $f(x)$ is the field at position x, n is the number of points we are averaging over, Q_n is the field at nearest neighbour n, and W_n is the weight given to point n based on distance from x. W_n is given by,

$$W_n(x) = \left(\frac{R_x - ||x - x_n||}{R_x ||x - x_n||} \right)^2 \tag{3.20}$$

where $R_x = \max ||x - x_n||$, the distance between x and the furthest of the nearest neighbours n.

3.7 Performance of Simulation

This section describes tests that the CryoEDM simulation has been checked against in order to confirm that the underlying algorithms produce the expected behaviour under certain well known situations. There are two main parts of the simulation under scrutiny here: the propagation of UCN under gravity and through material bottles, and

[3] https://en.wikipedia.org/wiki/Inverse_distance_weighting

the evolution of the UCN spinor under a magnetic field.

3.7.1 Effect of Gravity on Vertical Gradient in UCN Density

This test is based on a paper by J.M. Pendlebury and D.J. Richardson [15], titled 'Effects of gravity on the storage of ultracold neutrons'. A section of the paper discusses the effect of gravity on the real-space distribution of UCN in a bottle. Since UCN energies are so low, it is typical that gravity will bring a UCN to rest at heights of $\sim O(1)$m, and thus gravity can have a large impact on the distribution of UCN in a storage bottle.

The effect of gravity is particularly important for determining the distribution of UCN between multiple sections of a UCN bottle that are at different heights to each other (for example, in the CryoEDM apparatus the production volume is 30cm higher than the measurement bottle). In the absence of gravity the UCN would spread themselves between the various volumes according to the ratio of their volumes, however under gravity this no longer applies.

Pendlebury and Richardson consider a mono-energetic group of UCN, with total energy, ϵ, in the range $\epsilon + \delta\epsilon$, where $\delta\epsilon \ll \epsilon$. The height coordinate, h is defined to be zero where the UCN gravitational potential energy is zero, and all wall collisions are assumed to be elastic, so that the energies of the UCN will always remain within the range $\delta\epsilon$ for all times in the future.

By utilising the equilibrium condition, where after a short period of time the UCN will have spread themselves such that the phase-space density (the particles's real-space density $n(\epsilon, t, h)$, divided by the volume available to them in momentum space) has become uniform across the bottle, one is able to derive[4] the following expression for the real-

[4] A summary of the argument is as follows. Assuming elastic wall-collisions, we have $p^2/2m = E = \epsilon - mgh$.

space density as a function of height up the bottle,

$$n(\epsilon, t, h) = n(\epsilon, t, 0)\sqrt{\frac{(\epsilon - mgh)}{\epsilon}} \tag{3.21}$$

By replicating the conditions under which this formula applies and measuring the density of neutrons along the height of the bottle, we would expect to see a good agreement with the above formula.

The test geometry used is a vertically-orientated cylinder of height 1.8m and the UCN are all started with a *total* energy $\epsilon = 200\,\text{neV}$ so that they are able to reach the full height of the cylinder. The UCN are distributed uniformly throughout the cylinder to begin the UCN in a distribution that is closer to equilibrium. The bottom of the cylinder is aligned at $z = h = 0$ which is where the gravitational potential is defined to be zero.

All wall collisions were set to be completely specular, elastic collisions and with wall losses disabled. After 100s of propagation, we plot the number of neutrons per cylindrical slice z, as a function of height from the bottom of the cylinder,

---

Differentiating $E = \epsilon - mgh$ with respect to h, shows that the kinetic energies of the UCN will cover the same range $\delta E = \delta\epsilon$ for all h. Considering the available momentum space,

$$4\pi p^2 \delta p$$

the range δE gives a range δp by $\delta E = p\delta p/m$ which allows us to express the available momentum space as,

$$4\pi p^2 \delta p = 4\pi\sqrt{2m^3}\sqrt{E}\delta E = C\sqrt{(\epsilon - mgh)}\delta E$$

where $C = 4\pi\sqrt{2m^3}$. After the UCN have spread throughout the volume and reached equilibrium, the overall phase space density should be uniform across the bottle. The phase space density is given by the real space density, denoted $n(\epsilon, t, h)$, divided by the available momentum space volume, and thus this ratio should be equal for all heights,

$$\frac{n(\epsilon, t, h)}{C\sqrt{E(h)}\delta E} = \frac{n(\epsilon, t, 0)}{C\sqrt{E(0)}\delta E}$$

which can be rearranged to give the desired expression in 3.21,

$$n(\epsilon, t, h) = n(\epsilon, t, 0)\sqrt{\frac{(\epsilon - mgh)}{\epsilon}}$$

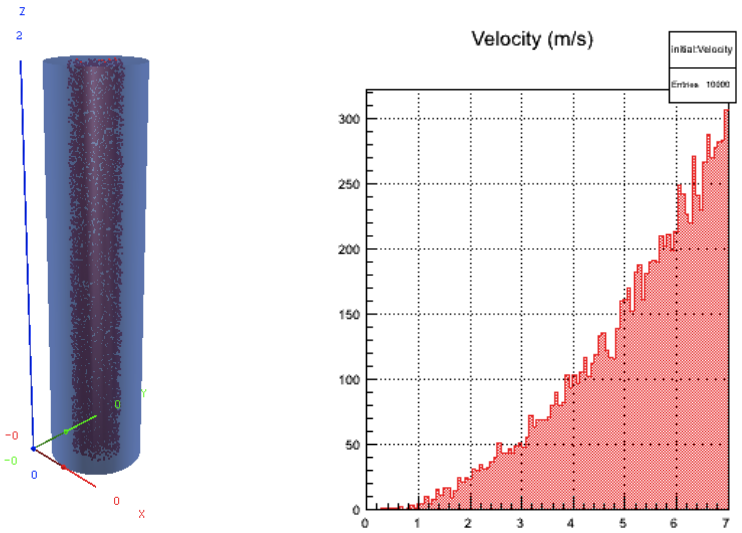

(a) Render of test volume

(b) Neutron velocity distribution (x-axis, m/s) vs neutron energy (y-axis, neV)

Figure 3.8: Figure (a) is a render of the test volume used in testing the particle motion under gravity. The gravitational field is orientated downward along the cylinder's principle axis. Figure (b) shows the velocity distribution that the simulation is started with - all neutrons are started with a total energy of $200, \text{neV}$

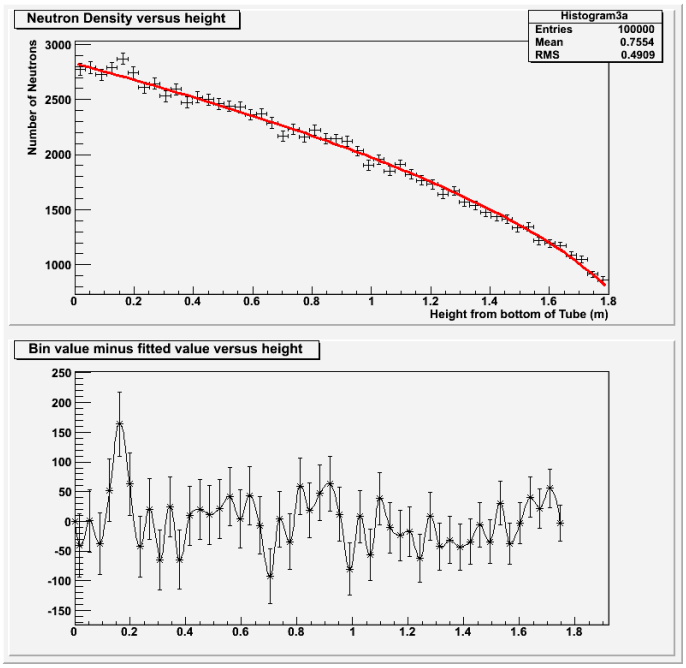

Figure 3.9: This figure shows a plot of the number of neutrons at each height (z) of the cylinder in figure 3.8 after a period of free propagation for 100 s. This distribution is plotted against the theoretical expectation (shown in red) of how they should be distributed under a gravitational field.

Figure 3.9 shows this plot fitted to the function in equation 3.21, which shows a good agreement with the theory.

3.7.2 UCN Loss-at-Boundary Probability

In this section we validate the simulation's calculation of UCN losses through the interaction with a material surface match the surface interaction physics that we expect.

In section 2.3.1.4 we re-derived the standard expression, equation 2.41, for the angular dependent probability of loss on reflection due to nuclear capture and inelastic scattering for a single UCN reflecting from a surface. In a less idealised case, the surfaces of a material bottle will not be perfectly smooth and there will be some fraction of reflections that are not specular, so that after a sufficient number of collisions the directions of the population of UCN will be randomly distributed.

Therefore one can integrate equation 2.41 over all angles of incidence to give the averaged loss probability per reflection, $\bar{\mu}(E)$,

$$\bar{\mu}(E) = 2\int_0^1 \cos(\theta)\,\mu(E,\theta)\,d(\cos(\theta)) \tag{3.22}$$

$$= 2f\left[\frac{V}{E}\arcsin\left(\frac{E}{V}\right)^{1/2} - \left(\frac{V}{E}-1\right)^{1/2}\right] \tag{3.23}$$

which approaches πf as $E \to V$, as shown in figure 3.10.

We can test this derivation in the simulation by using the same geometry as in the previous section, but re-enabling wall-losses and by setting all particle reflections to be completely *diffuse*. To reproduce this curve using the simulation we created 13 populations of monoenergetic neutrons, each with a different energy along the curve in 3.10 and then ran the simulation for 1000 s. For each population of

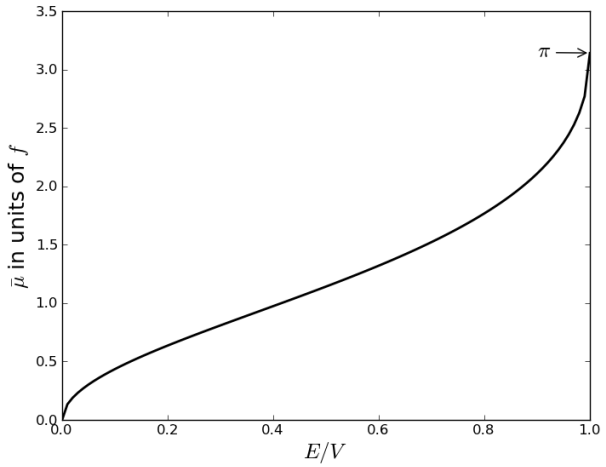

Figure 3.10: This figure is a plot of the angle-averaged loss-probability function (equation3.23) as a function of UCN energy (itself expressed as a fraction of the bottle wall's Fermi-potential).

neutrons of a particular energy, the mean number of reflections before a particle was eventually absorbed by the boundary was measured, and we then plotted $\bar{\mu}(E)$ as the inverse of this value. The simulated points are shown superimposed on the theoretical curve in figure 3.11,

The simulated points show a good agreement with the theoretical curve for most energies, although the fit becomes worse as the energy approaches that of the Fermi potential, however the particles make fewer collisions at higher energies so the statistics are also worse for these points.

3.7.3 Spin Precession under Magnetic Fields

This test uses a simple field map of a uniform magnetic field to measure the neutron spin evolution over time. For a perfectly uniform magnetic field aligned along an axis, Z say, we would expect UCN with spins initially polarised parallel to this field to remain completely polarised for all time. For UCN with spins initially polarised perpendicular to this field, we expect their spin to precess about this axis with frequency

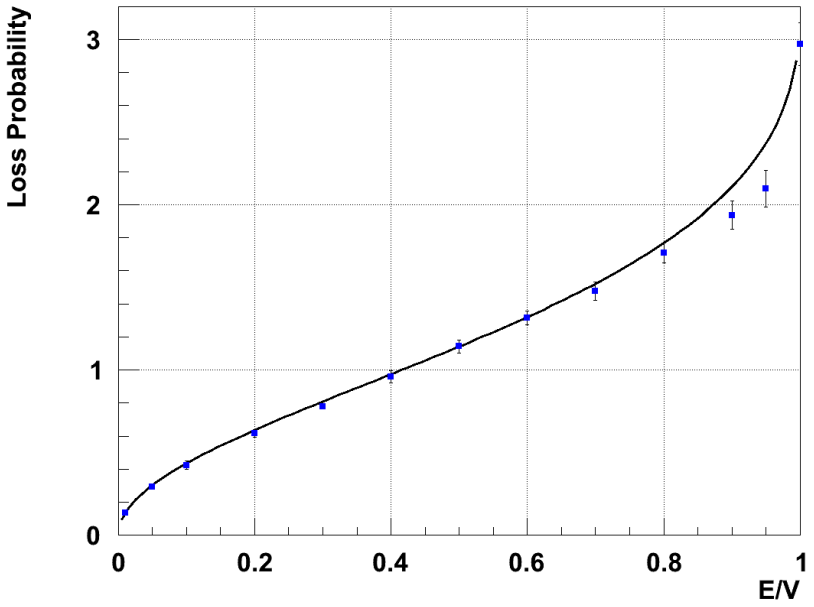

Figure 3.11: Calculated loss probability from simulations of UCN in a bottle at varying, fixed energies after for a fixed period of time. The loss probability in this case is just the fraction of those lost from the total and here is displayed as a function of the f, the loss factor, so that is can be plotted against the theoretical expectation.

given by the Larmour frequency.

A test of this is shown in figure 3.12, where we have simulated 1000 UCN in a simple cylindrical bottle with a uniform field map orientated along the z axis and have plotted the number of neutrons measured to be spin up and spin down as a function of time for a few milli-seconds. A sinusoidal curve with a frequency that matches that expected from the theory is shown superimposed over the data.

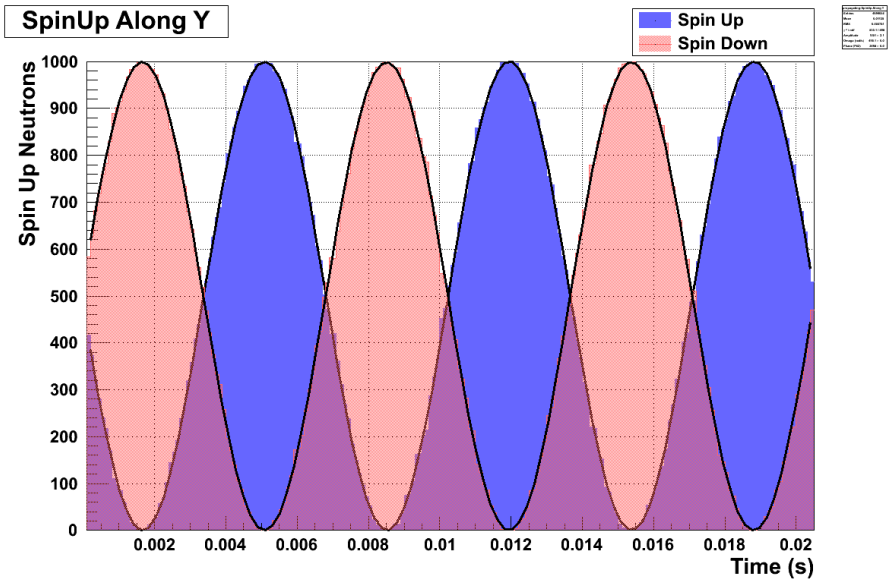

Figure 3.12: This figure shows a simulation of the Larmour frequency, tracking the evolution of neutron spin under a constant magnetic field. The magnetic field is orientated along the z axis, the particles are initially polarized perpendicular to the magnetic field and we are measuring the particles' spinor components along the y axis at a fixed period, and then using these to calculate the probability of the particle being spin up or down at that time. We then use a random number generator to 'decide' whether each particle would be spin up or down and show the results for 1000 neutrons, fitted to sinusoidal curves to check that their frequency matches the expected Larmour frequency.

4 Optimising the CryoEDM Magnetic Field

In order to attempt a measurement of the neutron EDM, we have to ensure that the static, holding magnetic field in the Ramsey cell is spatially homogeneous. During the summer of 2010, the CryoEDM collaboration decided to investigate the magnetic field of the Ramsey cell region of the apparatus as it was suspected that parts of the apparatus, in particular the superfluid containment vessel (SCV) might contain magnetic impurities that affect the static field's uniformity.

This chapter contains a description of experimental measurements taken on the CryoEDM apparatus at the Institut Laue Langevin of the field within the SCV at super-conducting temperatures. These measurements showed that the axial field gradient across the SCV was roughly two orders of magnitude larger than the collaboration's design specification.

To try to compensate for this inhomogeniety in the holding field, it was decided to explore whether a set of 21 correction coils mounted around the exterior of the SCV could be used to counteract the impurities detected. Professor P.G. Harris, K. Katsika and myself, developed a systematic method to determine an optimal set of currents that could be applied to these coils to minimise the field inhomogeneity. This required further measurements to characterise the response of all the coils, as the presence of three μ-metal shields in close proximity was expected to modify their field from the theoretical expectation.

This chapter also describes a new piece of software developed to perform the optimisation analysis mentioned above, along with further experimental measurements taken to measure the effects of the coil configurations that the software recommended.

Lastly, the Monte Carlo simulation was used to determine the effect of the measured fields on the neutrons' depolarisation lifetime T_2 to predict whether the magnetic field could be used to perform a Ramsey resonance. This work demonstrated that our work to use the compensation coils to improve the static magnetic field's homogeneity could improve the length of T_2 by an order of magnitude, up to roughly 20 s.

4.1 Description of the Experimental Setup

In this section we describe the relevant changes to the experimental apparatus that were made to enable us to carry out a detailed scan of the static magnetic field across the Ramsey cell region.

The purpose of the experiment was to measure the magnetic field across the SCV at close to operating temperature in order to determine whether the field gradient was sufficiently low to allow a future cool-down to perform a Ramsey resonance experiment. A similar measurement was first performed in January 2005 with only the solenoid and superconducting shields installed, however, crucially, the SCV was not present at that time.

The current apparatus uses a stainless steel (316L) SCV, and there exists a possibility of this material, or welds along the SCV having magnetic properties that may affect the magnetic field gradient in the SCV. Therefore before attempting to conduct a magnetic resonance experiment, the collaboration decided to carry out two tests of the

SCV:

1. Firstly, measure the magnetic field properties of just the SCV itself, in isolation, at room temperature, carried out at Rutherford Appleton Laboratory (RAL).

2. Secondly, measure the magnetic field of the whole assembled apparatus, mounted on-site at the experiment in ILL, cooled to base temperature.

The room-temperature experiment at RAL was a much simpler set-up than the full experiment, consisting of a single 3-axis fluxgate magnetometer fixed in position, while the SCV was mounted on a non-magnetic set of rails which enabled the SCV to be moved over the fluxgate. Two sets of measurements were made, one where the the trolley is positioned so that the fluxgate measures the field along the central axis of the SCV, and another where the fluxgate was positioned 4cm off-axis.

4.1.1 Magnetometer Array

For the 'cold' ILL scan of the SCV magnetic field, the original apparatus from the January 2005 cooldown was used [16]. This consisted primarily of a long perspex tube running along the central axis of the SCV, with a short, radial-arm piece on which are mounted 3 single-axis fluxgate magnetometers at different radii: one fluxgate was positioned on axis at $R = 0\,\mathrm{cm}$, another at $R = 7.5\,\mathrm{cm}$ and the third at $R = 15\,\mathrm{cm}$.

The plastic tube was designed to be fed through each of the two baseplates and be able to slide along the z-axis as well as be able to be rotated so that the fluxgate arm could measure the magnetic field inside the SCV at various z and θ. To facilitate this, a support struc-

ture of metal bars was mounted around the protruding end of the perspex tube, and onto which notches were drilled to enable the tube to moved along z by a maximum extent of 50cm with a precision of 2 cm increments.

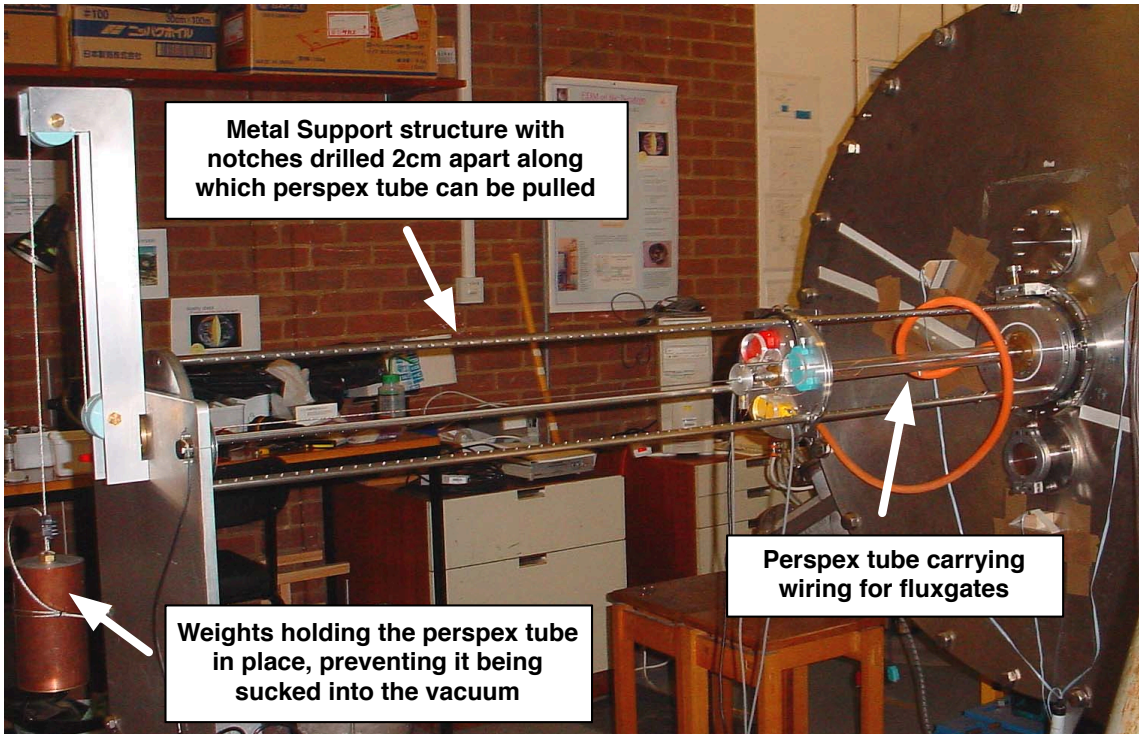

Figure 4.1: The magnetometer array as it appears from outside the SCV, when it was assembled for testing. This shows mostly the metal support structure that was used to move the fluxgates housed inside the SCV. The plate with the red, blue and yellow cases on contain wiring for the three fluxgates, which then runs down into a perspex tube and through a seal on the experiment's base-plate into the SCV. This plate could be moved horizontally by 2 cm increments, as well as rotated 360° in 15° increments.

The support structure also had 24 notches drilled about θ, enabling the tube to be rotated with a precision of 15° increments. Potentiometers were also mounted to measure the precise z and θ positions of the magnetometers.

An additional two magnetometers were added to this set-up over the 2005 scan. One magnetometer was mounted inside the perspex tube, on axis, but positioned a further 50 cm along the tube from the radial arm, towards the 6-way section end of the SCV. The other was fixed

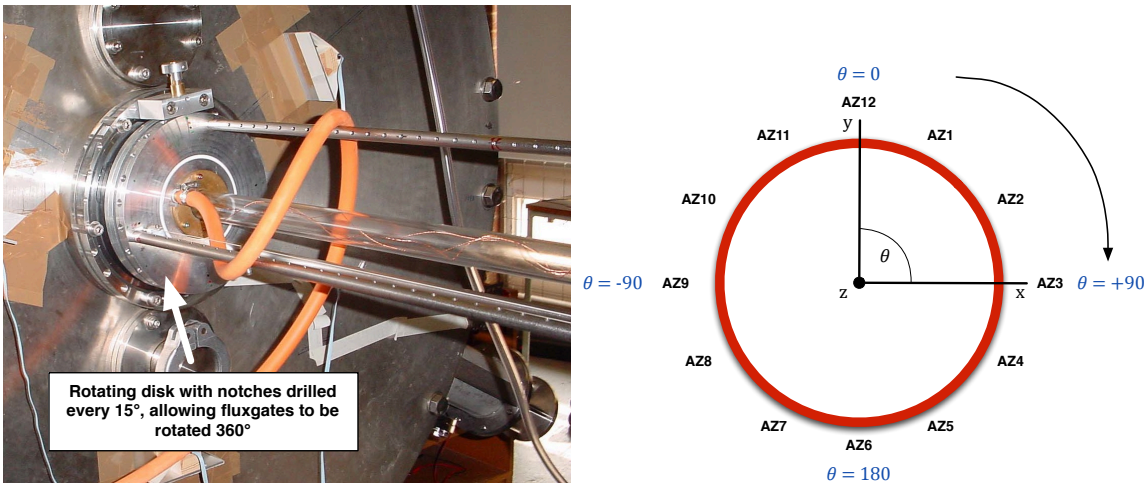

(a) Red (b) Yel

Figure 4.2: Fig shows a close up view of the rotating disk with the 24 notches marking the various angular positions the fluxgates could be locked at when performing a measurement. Fig shows the labelling scheme of the 12 azimuthal compensation coils as they map to the angle of the rotating fluxgates.

in position outside the SCV in the G10 mounting ring to which the SCV is bolted, again, at the 6-way section end.

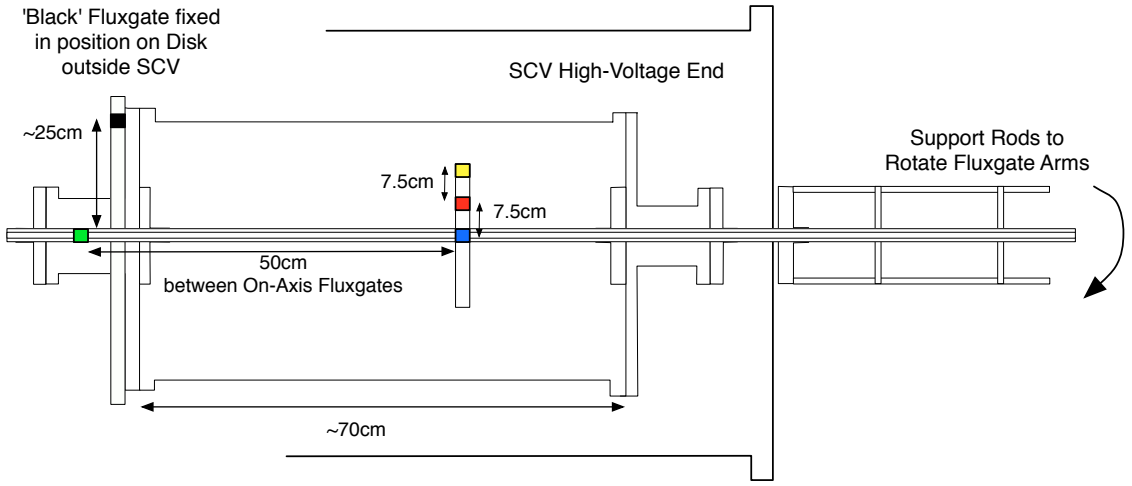

Figure 4.3: A cross-section of the experiment showing the location of the fluxgates inside the SCV on the rotating arm, shown by the colours that they came to be named after (due to the colours of the wiring cases in fig 4.1). Also shown are two other fluxgates, the 'black' being mounted statically on the outside of the SCV and the 'green' within the perspex tube but offset from the other fluxgates by 50cm so as to measure the field through the base-plates.

The magnetometers were Bartington low temperature single-axis fluxgate probes (type 'F') connected to Bartington Mag-01H control units. The sensitivity of these magnetometers is quoted by the manufacturer

as 0.1 nT [16].

4.1.2 Compensation Coils

To correct for the azimuthal variation in the field, a set of compensation coils was designed by Professor Mike Pendlebury. The coils are wound on a cylindrical carbon-fibre forma that fits directly around the outer surface of the SCV and has a radius of 0.265 m. Twelve azimuthal correction coils were wound onto the former along with an additional seven *axial* compensation coils that could be used to further improve the axial magnetic field gradient within the Ramsey cells.

The azimuthal correction coils are paired saddle-coils. Each coil in the pair has the same r and θ coordinate, but different z-positions along the forma as shown in figure 4.4. Each coil in the pair was wired so that the current went through each loop in the opposite sense to the other, producing flux lines that enter the forma through one loop and exits the forma through the other loop. The saddle coils are aligned symmetrically with respect to the vertical plane of the forma, and thus the flux lines in the centre of the forma are aligned parallel to the z-axis, parallel to the solenoid holding field.

With 12 azimuthal compensation coils, each pair subtend an angle of 30°.

The axial compensation coils are simply additional circular coils wound around the forma. The seven coils are positioned symmetrically around the centre of the forma, with one coil at $z = 0$ and the remaining six at ± 11 cm, ± 21 cm, ± 31 cm.

For this run, all 19 compensation coils were wired independently to seperate power-supplies so that each coil's current was a free parameter to be determined.

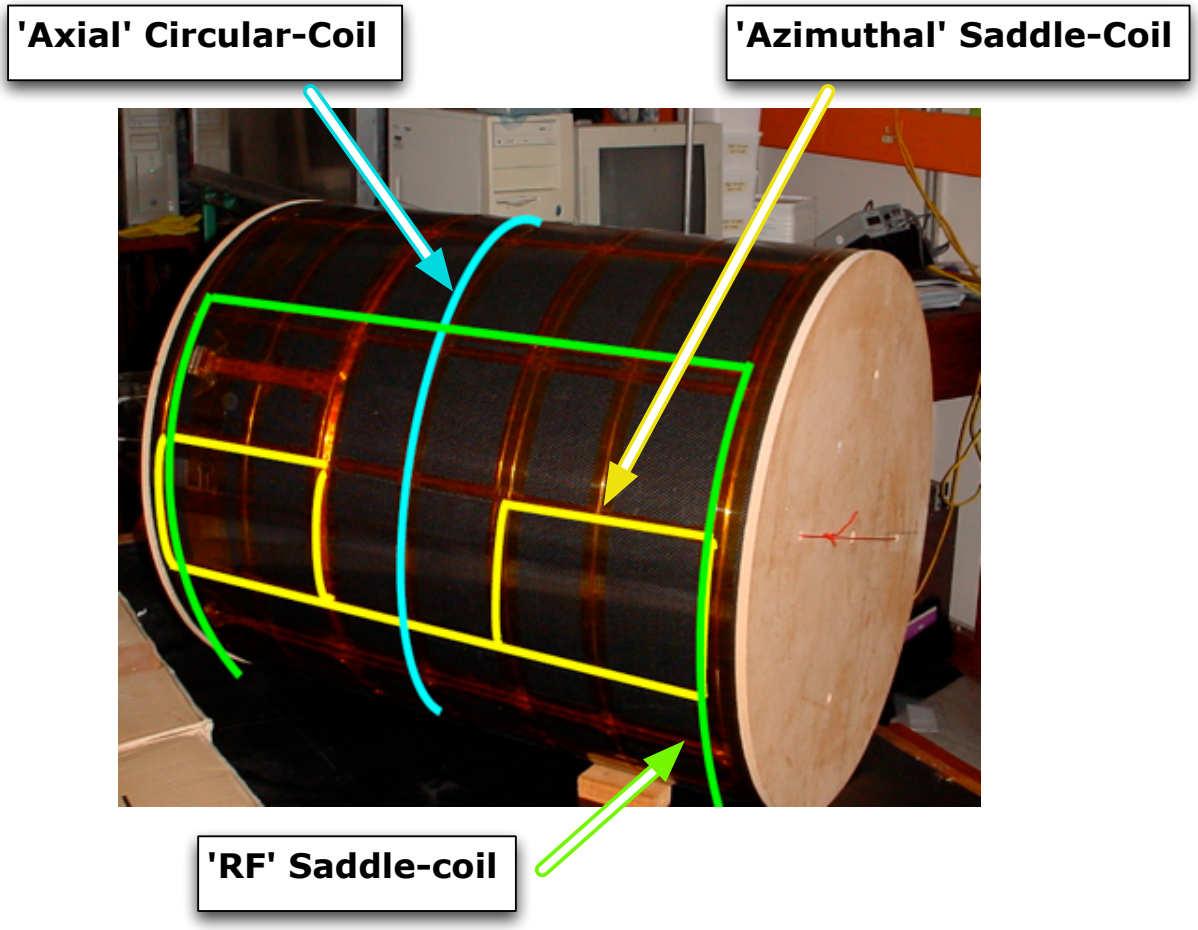

Figure 4.4: Diagram of the shape of the azimuthal compensation saddle-coils mounted on the carbon-fibre forma

4.2 RAL Measurements of SCV

The on-axis measurements of magnetic field inside the SCV and baseplates is presented in figure 4.5.

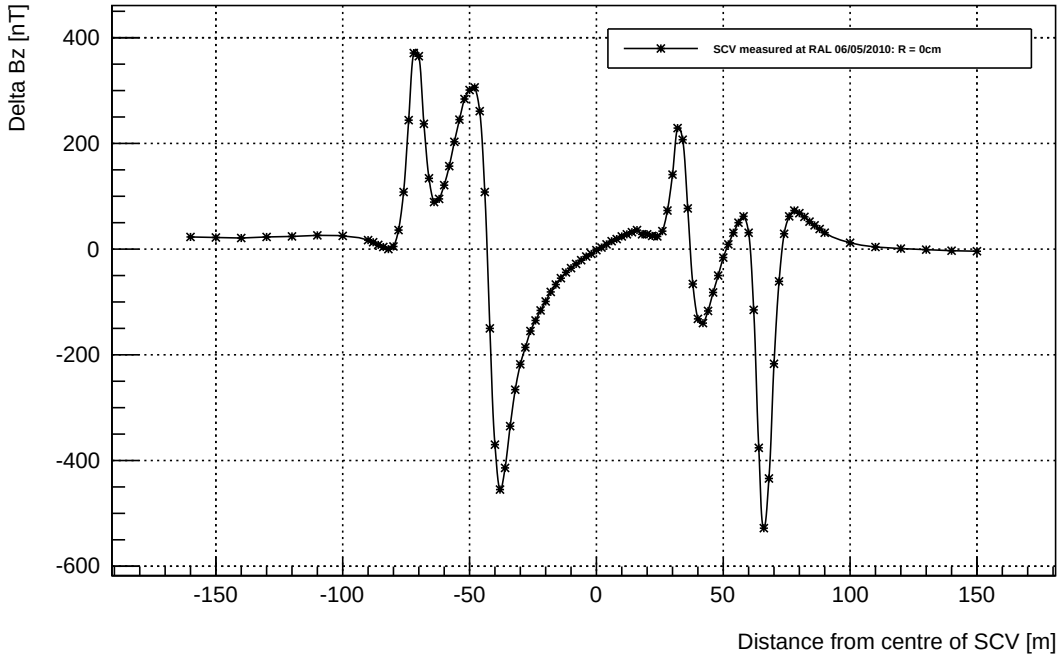

Figure 4.5: Room-temperature measurement of the magnetic field, measured at $R = 0$cm, through the SCV. The x-axis shows distance measured from the centre of the SCV and the region containing the Ramsey cell starts from approximately $x = -30$cm to $x = +20$cm. The two large peaks at approximately $x \approx -80$cm and also at $x = +70$cm correspond to the locations of the SCV baseplates.

There are three distinct regions to this plot. The left-most region is where the probe passes through the baseplate on the end of the SCV where neutrons enter to the Ramsey cell region, and at this point there is a large fluctuation in the field. The central region of the plot shows a smoother, but still significant gradient in the field and it is in this region that the Ramsey cells are situated. Finally on the right of the plot are further large fluctuations in the field, again corresponding to the probe moving through the baseplate at the other end of the SCV, where the high-voltage supply is usually situated.

The gradient across the Ramsey cell region is of the order 300 nT/m which is about two orders of magnitude larger than our field requirements. The conclusion then is that some part of the SCV, either impurities in the stainless steel used, the welds around the SCV, or its flanges, have magnetic impurities that are causing these anomalies in the axial magnetic field.

4.3 ILL Measurements of SCV

At ILL, with the SCV mounted inside the horizontal shields and solenoid, the axial magnetic field across the SCV was measured multiple times as the apparatus was slowly cooled down to the temperature that the magnetic shields go superconducting over a period of weeks. This allows us to compare these measurements against those made at RAL; in figure 4.6 we compare the RAL measurements against the ILL measurements at room temperature.

As expected the room temperature ILL measurements show the same fluctuations as seen in the RAL data.

In order to investigate the SCV field anomaly further we examine the axial field measurements at various key temperature points on the way to 'base' temperature to determine whether the fluctuations change with temperature.

As shown in figure 4.7, the magnetic field fluctuations remain the same as the temperature falls all the way to 10K, with the same magnitude of the axial gradient across the Ramsey cell region.

With the full complement of Fluxgate magnetometers we have in the ILL system, we are also able to look at the magnetic field as a function of θ and at the two off-axis radii of 7.5 cm and 15 cm. In figure 4.8

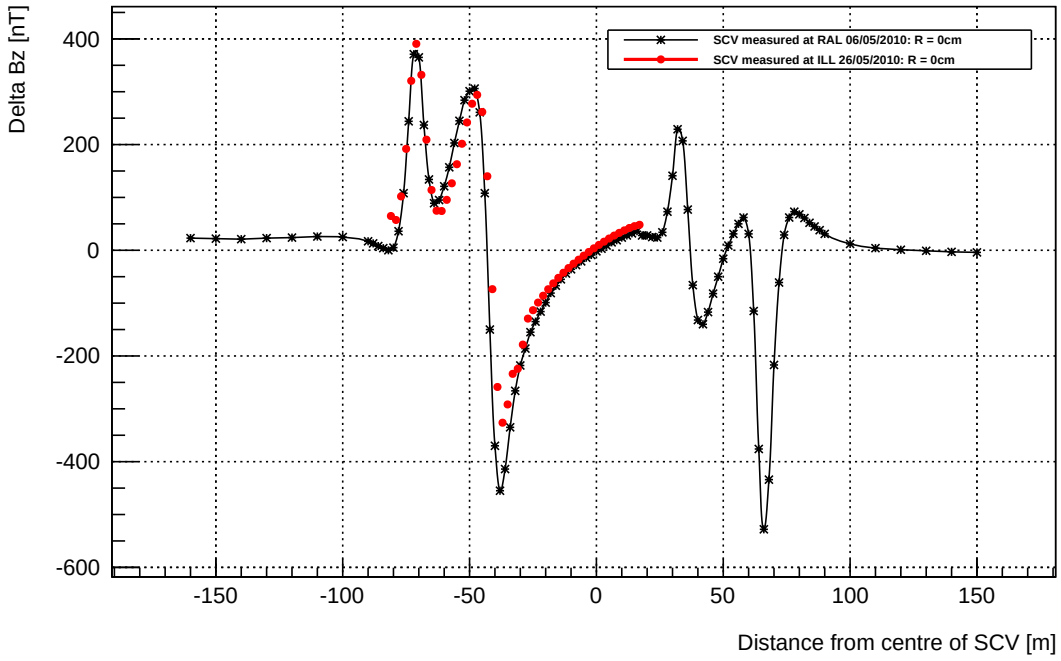

Figure 4.6: Measurements of the axial magnetic field taken at the ILL at room temperature superimposed on top of the measurements taken at RAL. The measurements show the same broad magnetic features and gradient across the ramsey cell region.

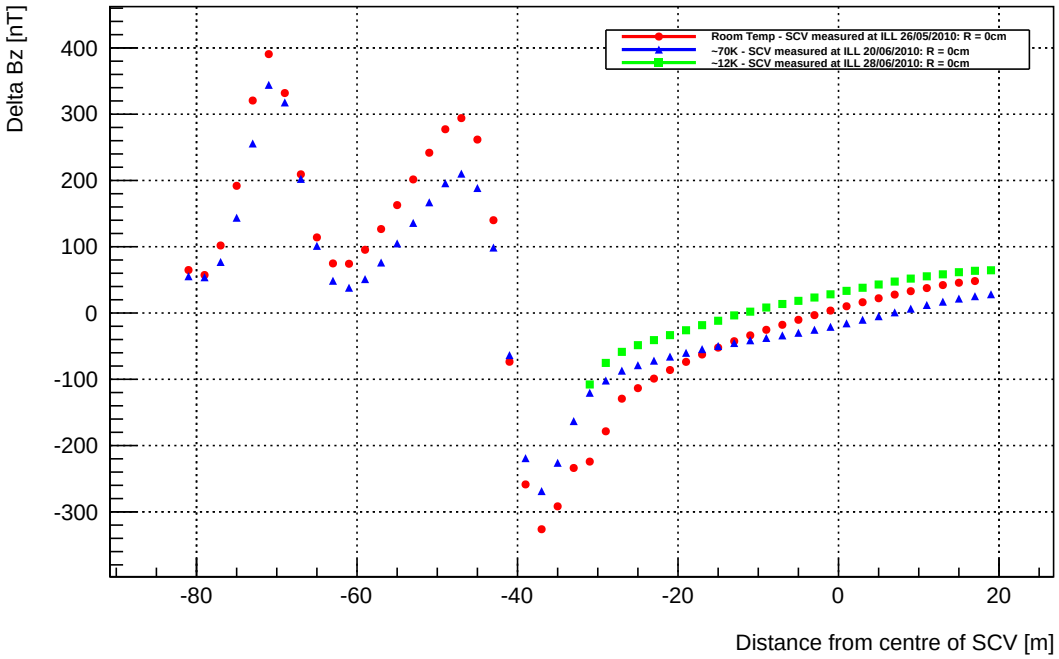

Figure 4.7: Axial field measured at ILL at three different temperatures as the apparatus is cooled down to base temperature. The Red points are the room temperature measurements, the blue correspond to $\approx$ 70K and the green points correspond to $\approx$ 12K. What is interesting is the lack of significant change in the gradient or magnetic features as the temperature is cooled by such a large amount.

are 2D surface plots of the axial magnetic field B_z as a function of distance from the centre of the SCV, z, and angle about the SCV, θ, where $\theta = 0$ represents 'up', the vertical axis.

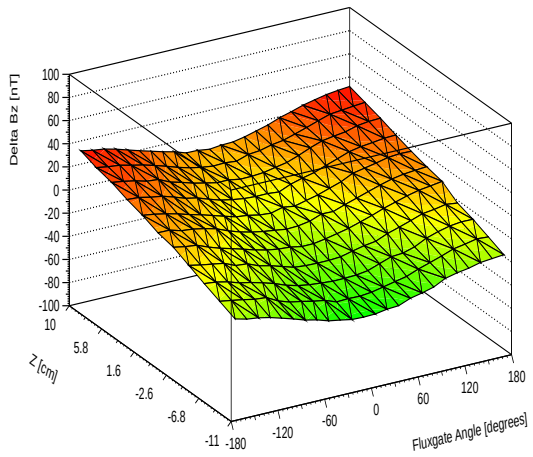

(a) Blue

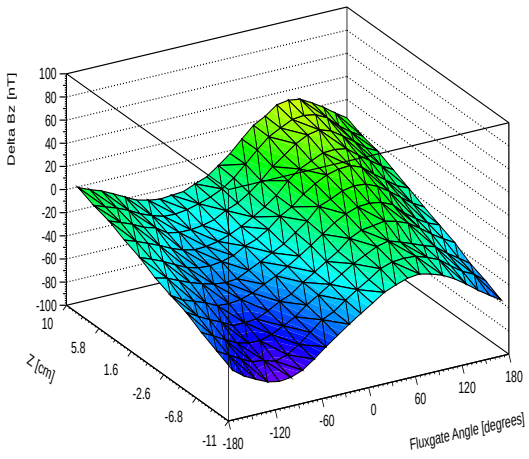

(b) Red

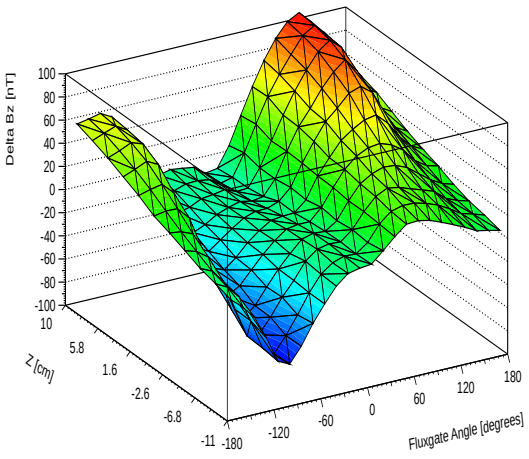

(c) Yel

Figure 4.8: Contour plots of the field as a function of axial distance (Zcm) and angular rotation (θ) as measured by the fluxgates and interpolated to give a smooth 'contour'. Figure 4.8a represents the field measured by the 'blue' ($R = 0$cm) fluxgate, figure 4.8b is the 'red' ($R = 7.5$cm) Fluxgate and figure 4.8c is the 'yellow' ($R = 15$cm) Fluxgate. Notice that as you move further out in radius the size and location of the magnetic inhomogeneities changes substantially, suggesting some specific regions of the SCV are to blame.

4.4 Optimisation Principle

This section describes both the method and implementation of a routine to find a configuration of the compensation coils around the SCV that will reduce or eliminate the gradient of the magnetic field across the Ramsey cell region. With 19 compensation coils, and a large amount of data on the magnetic field across this region, finding the optimal configuration of these coils is not a trivial process and cannot be done by trial-and-error.

However, if we make the reasonable assumption that the magnetic field produced by each of the compensation coils is *linearly* proportional to the current through the coil, then the field-compensation problem can essentially be reduced to a problem of linear function minimisation.

At any point in space inside the SCV, $\vec{r}$, the magnetic field is

$$\vec{B}(\vec{r}) = \vec{B}_S(\vec{r}) + \sum_{k=1}^{N_c} I_k \vec{f_k}(\vec{r}) \tag{4.1}$$

where $\vec{B}_S$ represents the static field inside the SCV, such as that produced by the solenoid and the SCV itself, as well as any other contributions such as from the guide-field coils and indeed the earth's magnetic field; N_c represents the number of compensation coils; I_k represents the current of compensation coil k; and $\vec{f_k}$ are the constants of proportionality, or 'coil responses', that relate the field produced by compensation coil k to its current at each point in space.

In principle these constants $\vec{f_k}$ can be calculated given the dimensions of the coil and calculating the field produced by such a coil in isolation, in free-space, however since these coils are situated inside a superconducting shield, this is not easy to do. Thus it is simpler in fact to measure these coil responses experimentally by activating each

trim coil individually, for a number of different currents at each point in space that our scan apparatus allows. In this way, for each point in space we can measure, we can extract the (linear) response $\vec{f_k}$ of the each coil.

Since our fluxgate magnetomers only measure the z component of the field, we shall drop the vector notation, leaving us with only a single equation from 4.1,

$$B(i) = B_S(i) + \sum_{k=1}^{N_c} I_k f_k(i) \tag{4.2}$$

where the index i represents the discreet measurement vertices of our apparatus.

We define the function to be minimised as,

$$\chi^2 = \sum_{i=1}^{N_p} \left(\frac{B(i) - B_0(i)}{\sigma(i)} \right)^2 \tag{4.3}$$

$$= \sum_{i=1}^{N_p} \left(\frac{B_S(i) - B_0(i) + \sum_{k=1}^{N_c} f_k(i) I_k}{\sigma(i)} \right)^2 \tag{4.4}$$

where B_0 is the 5 µT solenoid field; N_p is the number of spatial data points; and $\sigma(i)$ is the weighting given to point i. The reason why we subtract the solenoid field here from our original function for the magnetic field inside the SCV (equation 4.2) is that we don't want to minimise the *total* magnetic field inside the ramsey cells; we want to minimise the *fluctuations* away from the solenoid's field that reduce the field uniformity.

To simplify notation going ahead we make the substitution $B_\Delta(i) \equiv$

$B_S(i) - B_0$.

Then in the standard manner, we minimise our function, χ^2, with respect to each of the currents I_k,

$$\begin{aligned} \frac{\partial}{\partial I_m}\chi^2 &= 2\sum_{i=1}^{N_p}\left\{\frac{f_m(i)}{\sigma_i}\left[B_\Delta(i) + \sum_{k=1}^{N_c} I_k f_k(i)\right]\right\} = 0 \\ \rightarrow \qquad \sum_{i=1}^{N_p}\frac{B_\Delta(i)f_m(i)}{\sigma_i} &= -\sum_{k=1}^{N_c} I_k \sum_{i=1}^{N_p}\frac{f_k(i)f_m(i)}{\sigma_i} \end{aligned}$$

We thus have essentially N_c simulataneous equations to be solved for the currents I_k, that we can write in matrix form,

$$\begin{pmatrix} \sum_{i=1}^{N_p}\frac{B_\Delta(i)f_1(i)}{\sigma_i} \\ \vdots \\ \sum_{i=1}^{N_p}\frac{B_\Delta(i)f_{N_c}(i)}{\sigma_i} \end{pmatrix} = \begin{pmatrix} \sum_{i=1}^{N_p}\frac{f_1(i)f_1(i)}{\sigma_i} & \cdots & \cdots \\ \cdots & \cdots & \cdots \\ \cdots & \cdots & \sum_{i=1}^{N_p}\frac{f_{N_c}(i)f_{N_c}(i)}{\sigma_i} \end{pmatrix} \begin{pmatrix} -I_1 \\ \vdots \\ -I_{N_c} \end{pmatrix} \tag{4.5}$$

which we denote as,

$$\beta_m = -\alpha_{mk} I_k \tag{4.6}$$

where β_m is the column vector of elements,

$$\sum_{i=1}^{N_p}\frac{B_\Delta(i)f_m(i)}{\sigma_i} \tag{4.7}$$

α_{mk} is the matrix of elements,

$$\sum_{i=1}^{N_p}\frac{f_m(i)f_k(i)}{\sigma_i} \tag{4.8}$$

and I_k is the vector of currents. We then simply solve the N_c simultaneous equations for the optimal currents I_k, given by,

$$I_k = -\alpha_{mk}^{-1}\beta_m \tag{4.9}$$

After performing this procedure we can then easily test this configuration of compensation coil currents by performing another full scan of the field inside SCV and measure any improvement in the field homogeneity.

4.4.1 Measurement of Compensation Coil Response Parameters

We are only interested in optimising the magnetic field over the ramsey cell region of the SCV so the measurement vertices required will be those of the three central fluxgate magnetometers on the perspex tube's protruding arm. From the description of the magnetometer array in section 4.1.1, we know that with 15° increments there are 24 angular measurements made for each z position, and the array moves in 2 cm increments up to a maximum of 50 cm along z, giving 600 vertices for each of the three fluxgates, making 1800 vertices in total. However, the Ramsey cell region only covers a horizontal distance of at most, roughly 20cm, so if we only want to minimise the field variations in this region that would mean just 240 vertices per fluxgate, making a total of 720 vertices it total.

At each position of the apparatus, each of the 19 coils are turned on individually to 4 different current settings by the magnetometry computer: 0 mA, −20 mA, 20 mA, and back to 0 mA (we measure 0 mA again at the end to see if there is any offset from the initial reading, which would indicate that we would need to repeat the measurement as the background field environment has changed).

Despite being automated by the magnetometry computer, this process takes approximately 10 minutes for each position, since each fluxgate measurement for each current setting was averaged over a period of a few seconds. This, alone, adds up to 40 hours to cover all the positions, without taking into account other practicalities such as the time to move the apparatus to the next position, as well as the inevitable loss of time from personnel change-overs.

The eventual measurement ran over the 2nd, 3rd and 4th July 2010, and covered only 184 positions of the total planned 240 positions. This was due in part to time constraints, as the apparatus was due to be warmed up a week later, however it was felt that sufficient data had been collected by then for the optimisation process to be carried out.

The 184 positions consisted predominantly of all 24 angular positions across a 12 cm region about the centre of the SCV (z positions of $0, \pm 2, \pm 4, \pm 6$ cm), making up 168 positions. The remaining 16 vertices covered the 4 angles $0°, 90°, 180°, 360°$ at z positions of ± 8 and ± 10 cm. These positions cover the ramsey-cell region sufficiently, since each cell in the 2-cell design is 4.5cm in width, separated from each other by just 1.5cm.

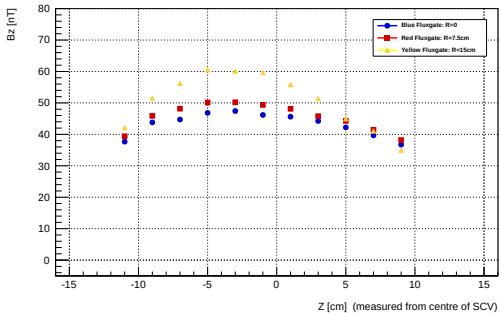

(a) AX4 +20mA

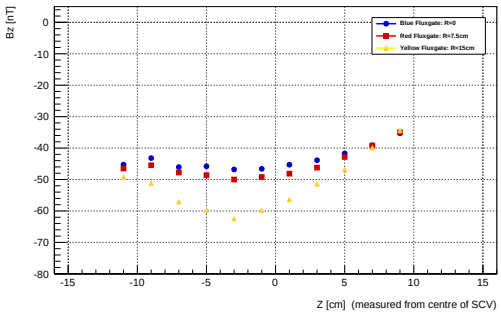

(b) AX4 -20mA

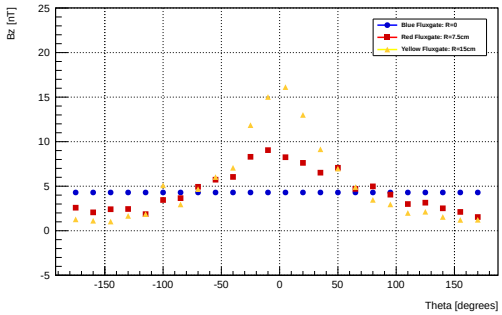

(c) AZ12 +20mA

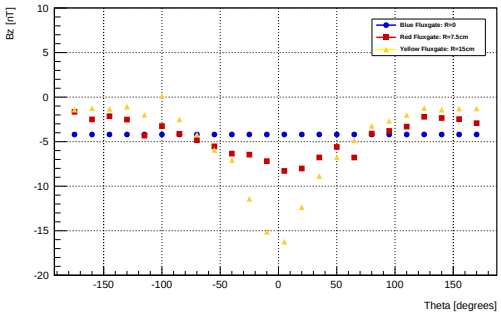

(d) AZ12 -20mA

Figure 4.9: These plots show 4 examples of the fields produced by the compensation coils across the centre of the SCV for the three radial fluxgates. Each plot has three sets of points, blue, red and yellow for the three fluxgates at $R = 0$, 7.5 and 15cm respectively. For plots 4.9b and 4.9a, the y-axis is the field measured in nT and the x-axis is distance from the center of the SCV, running from roughly $\pm$10cm. Fig 4.9a shows the Axial coil AX4 powered with +20mA which shows a peak at approximately -5cm and is broadly similar shaped for all fluxgates. Fig 4.9b shows the same coil but with the current reversed to -20mA. Fig 4.9c and 4.9d show $\pm$20mA respectively for the AZ12 azimuthal coil with the x-axis showing θ. AZ12 was mounted close to $\theta = 0$ and we see this as there is a large peak in the yellow points corresponding to the $R = 15$cm fluxgate, at $\theta = 0$.

I wrote a small program to calculate the response of each coil at every point from the above data, by simply fitting the measurements as a function of current applied to a straight line. This fitting process also confirmed our original assumption of linearity, as expected. An example of the fields produced by some of the coils is shown in figure 4.9.

The output of this program was a table of linear response factors

for each coil at each of the $184 \times 3 = 552$ vertices covered by the fluxgates.

4.5 Optimisation of Measured Field

To perform the optimisation itself I wrote a C++ program to read the experiment's data files and perform the analysis outlined above. The program solves equation 4.6, outlined in section 4.4, analytically by using the mathematical libraries of the ROOT C++ data analysis framework to perform the matrix inversion. This calculation has also been independently verified by solving the equation using functions to solve systems of linear equations within National Instrument's Labview software package (`www.ni.com/labview/`).

The optimisation program takes as its basic inputs the ASCII encoded data files from the compensation coil response scan described in section 4.4.1, as well as the data file from a scan of the residual SCV field that we wish to optimise, such as those described in section 4.3.

A number of important manipulations were applied to these files due to errors input to the DAQ software when measuring the data, and that need to be corrected before they can be used in the analysis.

4.5.1 Errors in Recorded Data

The position and angle of each measurement was, unfortunately, largely entered manually by the operators into the Oxford Magnetometry software, as the potentiometers installed to record this data were unreliable, despite numerous attempts to calibrate them. This led to numerous errors in the data files as positions were often input incorrectly, or duplicate points were recorded. These errors were recorded in the experiment's logbook and are incorporated into my C++ program used

to analyse the data.

4.5.2 Calibration of Fluxgate Arm Position

Besides individual errors specific to each run, the angle of the fluxgate arm that is recorded in the file also needs to be adjusted to correct systematic offsets in the values input by the experiment operators. The angle was measured externally, by simply counting the notches in the rotating disk as obviously we cannot see the fluxgate arm from outside. When the magnetometry apparatus was installed prior to the run, the fluxgate arm was initially set to the vertical position, and this notch was recorded on the rotating disk.

This notch served as the zero of our angular measurements and as the disk was rotated, angles were measured by counting the notches away from this point (the markings can be seen in Figure 4.2). The convention chosen was to measure angles along the interval $(-180, +180]$, where positive angles are measured as the disk is rotated in an anticlockwise direction (for example in Figure 4.2 the disk has been rotated anticlockwise and appears to be one notch away from $+180^\circ$, making the angle $+165^\circ$). The reason for this convention was because the disk could not be rotated by 360° due to the various wires attached to the perspex tube, so this convention made recording the angle a natural fit with how the system was physically rotated.

However after cooling the apparatus to base temperature, the position of the fluxgate arm was shifted away from the vertical offset by approximately $+20^\circ$. This was calculated by analysing at what angle each of the azimuthal compensation coils around the SCV produced its maximum field on the yellow fluxgate. Since we knew relatively accurately the arrangement of the compensation coils, the angle at which coil AZ12 produced a maximum was the 'real' zero, and thus

from this we could calculate the offset from our recorded angle.

All data after the 22nd of June 2010, has a different offset for the angle however, as an incident with the perspex tube on that date, led to the another shift in the orientation of the fluxgate arm. All angular data after that date has an offset of $-55°$.

4.5.3 Optimisation Configurations

The optimisation program also supports adding weights to individual points. Common to all of the optimisation configurations used for the following analysis is to down-weight the measurements from the blue fluxgate by a factor of 1/24, since it is on-axis and thus at every angle we make essentially the same measurement.

Additionally, the program supports fixing particular coil parameters in the fit to particular current values or just to zero. If the parameter is fixed to a non-zero current, the program will attempt to use the coil response factors, to calculate the predicted effect of that coil setting and add that to the field to be optimised.

In total, five separate optimisation configurations were tested experimentally in the summer 2010 cool down. In each case, once a set of compensation coil currents were found, the apparatus was warmed up to a temperature just above the super-conducting transition temperature of the solenoid and lead shields, the shields were de-magnetised and the current configuration was applied, before the system was cooled back below the solenoid's transition temperature.

A short summary of the parameters used, is shown in the following sections. Where a comparison is made to the predicted field, we are again using the coil response factors to calculate the field contribution produced by each coil and summing these to give a predicted field

map.

For all configurations the large solenoid trim coils had their currents fixed.

Config No.	Date	Comment
(Base Field) 0	07/06/10	No compensation coils applied. Solenoid and Guide Field ON.
1	07/07/10	Axial Coils only
2	07/08/10	Azimuthal coil currents fixed by hand.
3	07/08/10	Similar to Config 2. but no longer using outer fluxgate in fit
4	07/09/10	No paramters are fixed
5	07/09/10	Currents same as Config 4. but with +10% to all axial coils currents

Table 4.1: Summary of the coil configurations tested

Configuration No.	0	1	2	3	4	5
AX1 (mA)	0	-24.1	103.7	-46.63	-44.4	-48.87
AX2 (mA)	0	-5.17	-29.515	2.695	6.64	7.3
AX3 (mA)	0	-9.18	-27.802	-4.25	-12.1	-13.3
AX4 (mA)	0	2.78	-19.345	-1.21	-9.99	-10.99
AX5 (mA)	0	4.73	-0.08	1.522	0.3	0.33
AX6 (mA)	0	8.99	-4.153	12.989	6.74	7.42
AX7 (mA)	0	-9.89	90	-6.387	0.4	0.44
AZ1 (mA)	0	0	18	18	-6.94	-6.94
AZ2 (mA)	0	0	20	20	87.9	87.89
AZ3 (mA)	0	0	20	20	30.16	30.16
AZ4 (mA)	0	0	18	18	22.47	22.47
AZ5 (mA)	0	0	0	12	43.63	43.63
AZ6 (mA)	0	0	0	20	3.07	3.06
AZ7 (mA)	0	0	0	-12	35.2	35.16
AZ8 (mA)	0	0	-18	-18	-4.15	-4.15
AZ9 (mA)	0	0	-20	-20	-43.54	-43.55
AZ10 (mA)	0	0	-20	-20	-28.8	-28.83
AZ11 (mA)	0	0	-18	-18	8.37	8.36
AZ12 (mA)	0	0	13.878	-5.651	25.41	25.41
6WS TC (mA)	-10	-10	-10	-10	-10	-10
HV TC(mA)	-12	-12	-12	-10	-12	-12

Table 4.2: Coils settings for the base field and the five 'optimised' configurations. Parameters that were fixed in fitting are signified by an orange background ... mA.

	Weightings $1/\sigma^2$			Resulting χ^2
Configuration No.	Blue Fg	Red FG	Yellow FG	
0	N/A	N/A	N/A	1
1	1/24	1	0	2
2	1/24	1	1/4	3
3	1/24	1	0	4
4	1/24	1	1	5
5	N/A	N/A	N/A	6

Table 4.3: Weight factors for the three fluxgates.

Configuration 1

This configuration focused solely on the axial compensation coils and fixed all other coil currents to zero.

The weightings chosen for this configuration were the standard down-weighting of the axial measurements by a factor of 24, combined with removing the outer, yellow fluxgate's measurements from the fit.

Configuration 2

This configuration had AX7 fixed along with all of the Azimuthal coils besides AZ12. These values were chosen roughly by hand, by studying the field produced by the individual compensation coils and iteratively guessing, approximately what currents would provide a rough improvement to the azimuthal field homogeneity.

This configuration was a product of the experimental circumstances at the time; there was a very limited window of opportunity remaining within which we could carry out these experiments before the apparatus needed to be warmed back up to room tempertature.

Running the optimisation routine with no parameters fixed resulted in currents larger than the power supplies available at that moment could supply. This was later remedied in time for Configuration 4 with

a reshuffle of the available power supplies on-site.

Configuration 3

This configuration followed on from Configuration 2, with AZ5, AZ6 and AZ7 also fixed by hand, and also changing the point weightings provided to the fitting routine. In this configuration the points from the outer (yellow) fluxgate were not included in the fit, as it was thought that by excluding the larger and more complicated pertubations of the field at this radius might lead to a smoother, simpler fit.

Configuration 4

This configuration was the only 'free' fit, with no parameters fixed in the optimisation routine. The weightings were also changed again, now including the field points from the outer (yellow) fluxgate with no down-weighting, so they were included in the fit with the same weight as points from the middle (red) fluxgate.

Configuration 5

This configuration had the exact same currents as applied in Configuration 4, only with all the Axial coil currents increased by +10%. This was so that we could hopefully gain some insight into how changing a group of the coils together by a meaningful amount would impact the field.

4.6 Analysis of Measured Coil Configurations

The goal of this experiment was initially to measure the magnetic field inside the SCV so we could try to predict the depolarisation storage time of UCN with a future EDM experiment. This would allow us to determine whether an EDM measurement could be made with the experiment in its current state, and would provide a crucial quantity in determining how long UCN could be stored in the Ramsey cells, which further, is part of the calculation of the experiment's sensitivity to an nEDM.

We have thoroughly measured the field within the Ramsey cell region of the SCV in an environment that is a close match to operating appartus in a future EDM experiment. We have also measured the linear response of all of the 19 field compensation coils at hundreds of points across the Ramsey cell region and used these response coefficients to build a linear optimisation routine to try and predict what combination of coil currents would produce the smoothest field in this region. Finally we have measured 5 different configurations of compensation coil currents produced using the optimisation routine.

In this section we will summarise our analysis of these 5 coil configurations by using the simulation to try to understand the effect that these coils have on the UCN spin depolarisation lifetime.

4.6.1 T_1 Relaxation Time

In an EDM experiment the T_1 relaxation time characterises the rate at which the component of the neutrons spins parallel to the holding magnetic field (conventionally the z component) tends to decay exponentially to their thermodynamic equilibrium value (which would be

for the population to be completely depolarised).

$$P(t) = P_0 e^{-t/T_1} \tag{4.10}$$

This relaxation time is typically dominated by the neutron-surface interactions and is heavily dependent on the choice of surface material, as the nuclei of the surface material are in constant vibrational motion and thus the magnetic environment in this interaction is complex and can sometimes lead to the neutron undergoing a transition from high-energy to low-energy spin states.

Because of this, it is hard to numerically calculate without a detailed knowledge of the particle-surface interaction so alternatively, a probability of spin-flip per particle-surface interaction is usually provided as a parameter into Monte-Carlo simulations and adjusted on the basis of experimental measurements of this relaxation time.

Typically for Beryllium-Oxide surfaces, $T_1 \approx O(10^3)$ therefore T_1 is usually not the dominant limitation on UCN storage for an EDM measurement.

4.6.2 T_2 Relaxation Time

On the other hand, the T_2 relaxation time is highly dependent on the uniformity of the holding magnetic field in an EDM experiment, and thus is usually much more of a limitation on UCN storage than T_1.

T_2 measures the rate at which the component of the neutrons spins perpendicular to the holding magnetic field tends to the decay exponentially to their equilibrium state (which, again would be for the population to be completely depolarised). This is highly relevant to an EDM style measurement as the time between the two $\pi/2$ RF pulses, when the UCN spin vector has been 'kicked' by the first pulse into the

plane perpendicular to the holding magnetic field, is inversely proportional to the size of the EDM that can be measured. This time is of course limited by T_2 as for an EDM measurement we require the UCN spins to remain coherent during this period, therefore the longer T_2 the longer the time the UCN spins can be left to precess between $\pi/2$ pulses and the longer a potential EDM interaction with the electric field can be left to produce a phase difference between the UCN spins and the second $\pi/2$ pulse.

Inhomogeneities in the holding magnetic field will cause neutrons in different parts of the cell to precess at different resonance frequencies and cause the UCN spins to decay to their equilibrium, unpolarised state quicker. Ramsey derived a constraint on the uniformity of the holding magnetic field [17],

$$\Delta B_0 = \frac{1}{\lambda}\sqrt{\frac{v}{lT_s}} \tag{4.11}$$

where ΔB_0 is the variaton in the magnetic field across the typical dimension of the cell, l, λ is the neutron gyromagnetic ratio, v is the neutron's average speed, and T_s is the storage time of the neutrons.

If we take $v = 7\text{m/s}$, $T_s = 100\text{s}$ and l as the width of the ramsey cell $l = 0.45\text{m}$ then we get $\Delta B_0 \approx 2.2\text{nT}$ over the width of the cell. That would require a gradient of less than 5nT/m.

This calculation compares unfavourably with the currently measured gradient across the ramsey cell region of $\approx 300\text{nT/m}$. Turning this formula around, a gradient of $\approx 300\text{nT/m}$ would imply $T_2 \approx 0.005\text{s}$.

However a better way to compare this is to simulate the spin relaxation using the Monte-Carlo simulation. To do this, we needed a way to convert our field measurements from being solely measurements of only one component of the field, B_z, into a proper field map with all three components of the field. To do this we used a simple approximation

where, since $\nabla \cdot B = 0$, we will assume that any difference between B_z and B_{avg} has gone into the radial, B_r component (ignore any B_θ component to make it simple).

For the simulation geometry, I created a model that matched the dimensions of the two-cell Ramsey Cell design that is to be used in future EDM experiments (Fig: 4.10)

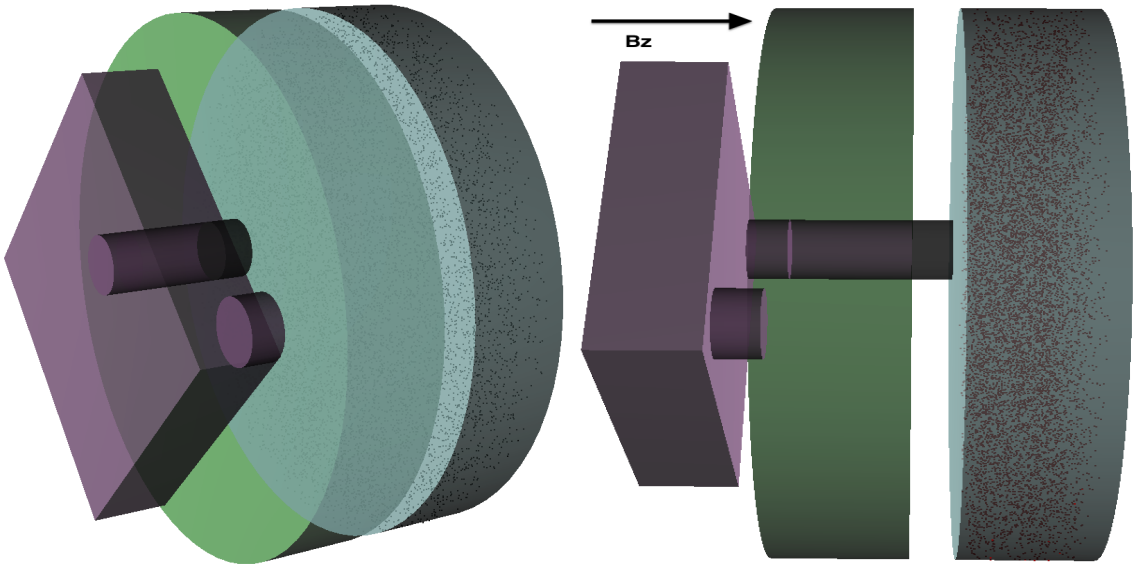

(a) (b)

Figure 4.10: Images from the Monte Carlo simulation showing a model of the ramsey cell from two different angles. Fig 4.10b shows from the side on the ramsey cell pre-volume with two holes leading to the two different chambers of the ramsey cell (only the right cell would have high-voltage applied). The small red dots are the neutrons simulated.

In the simulation, the UCN were confined to the HV-cell by closing the hole through the central electrode, and the field measurements from each configuration of the compensation coils was imported as a field map. In order to measure solely the effect of the static field's inhomogeneity, all mechanisms for UCN-loss in the simulation such as from wall collisions, were disabled.

Rather than simulate the effect of the rotating magnetic field pulses in this model, we will simplify the situation by initially polarising the

neutrons in the plane perpendicular to the holding field as though they had just undergone a $\pi/2$ spin transition from a single pulse of the rotating magnetic field. The neutrons are initialised with a uniform density across the Ramsey Cell region to start with. They are also initialised with a v^2 velocity distribution up to a maximum of 7 m/s, and their initial velocity vector is randomised in an even spherical distribution. I then simulate the neutrons for a duration of 100s typically and record every neutron's spin state (calculated quantum mechanically in this implementation, as a spinor evolving under the Schrödinger equation) at a frequency of 5Hz.

In order to compute the T_2 relaxation time in this case, I compute the population's polarisation along the holding field's principle axis at every measurement time. The polarisation should decay exponentially and T_2 is proportional to the rate of this decay.

To calculate each neutron's polarisation with respect to the field's (z) axis, for each spin measurement, we compute the projection of every neutron's spin state into the $x - y$ plane relative to the static holding field, and then calculate the angle these vector's make from the y axis (which I will refer to as their 'phase'). The average of all of these phases is computed and each neutron's 'phase-difference' from this average is computed. Given a perfectly uniform holding field, the average phase of the population should remain exactly $\pi/2$ out-of-phase with the rotating magnetic field, and thus, upon a second application of the rotating field will leave the neutrons spin-down (anti-parallel) relative to the holding field.

Inhomogeneities in the holding field though will cause the neutrons to gradually fall out of phase with the rotating magnetic field. We can picture this by plotting the distribution of neutron phases relative to the average at every spin measurement in the simulation. As the more spread out the neutrons become away from the average phase (which is

taken here to still be following the phase of the now gated-off rotating magnetic field) the more depolarised the population has become.

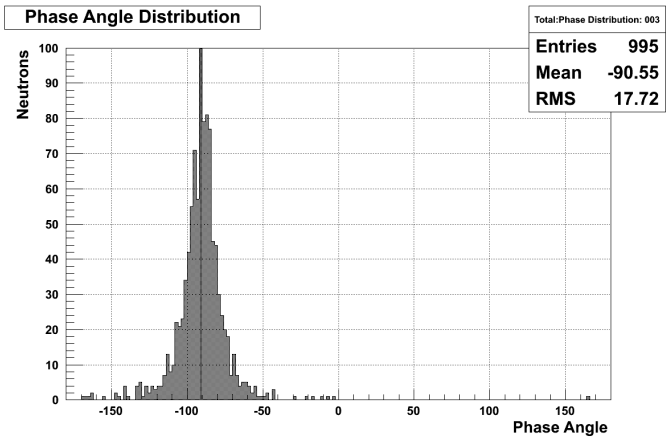

(a)

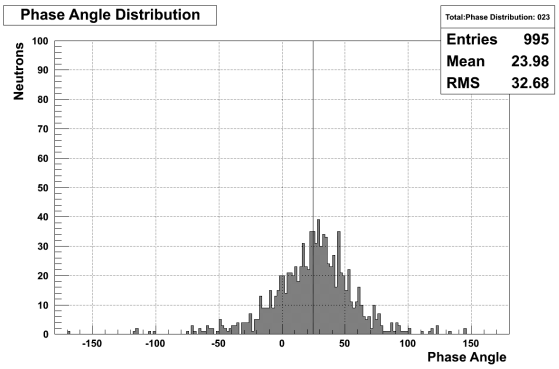

(b)

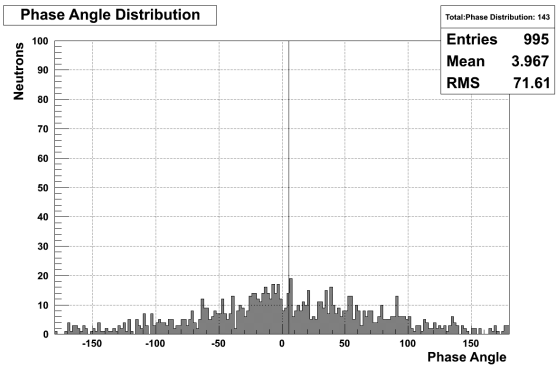

(c)

Figure 4.11: These plots show the distribution of the simulated neutrons phases at three different points in time as they are in the ramsey cell in the period of free precession after a $\pi/2$ pulse has just been applied to them. The x-axis shows the phase angle from $\pm 180°$ and the y-axis shows the number of neutrons. At this time their spin is in the plane perpendicular to the holding field and is precessing about B_z. High magnetic homogeneity would mean that the neutrons stay highly in-phase with one another and the rotating magnetic field that put them in this state, more like they are in 4.11a ($T = 0.5$)s. However as we see in 4.11b ($T = 1.5$s) and 4.11c ($T = 3$s), the magnetic inhomogeneities of our current field quickly cause all the neutrons to fall out of phase so that they become effectively de-polarised.

The difference between each neutron's phase and the average gives the probability of that neutron being spin down along the Z axis (the holding-field's principle axis) at every measurement time. The probability is given by,

$$P_{\downarrow} = \frac{\cos(\theta - \bar{\theta}) + 1}{2} \tag{4.12}$$

where θ represents each neutron's individual phase and $\bar{\theta}$ represents the population's mean phase.

The polarisation, denoted typically as α, is here taken to be,

$$\alpha_{\downarrow} = \frac{N_{\downarrow} - N_{\uparrow}}{N_{\downarrow} + N_{\uparrow}} \tag{4.13}$$

where $N_{\downarrow/\uparrow}$ represents the numbers of neutrons in the up or down spin states along the holding field's principle axis - effectively how many are in each spin state if we were to apply a second $\pi/2$ pulse of the rotating field at this point in time. Using the probability calculated from Eq.4.13 a random number generator is used to calculate how many are spin up/down and calculated α as a function of time, as shown in Fig. 4.12)

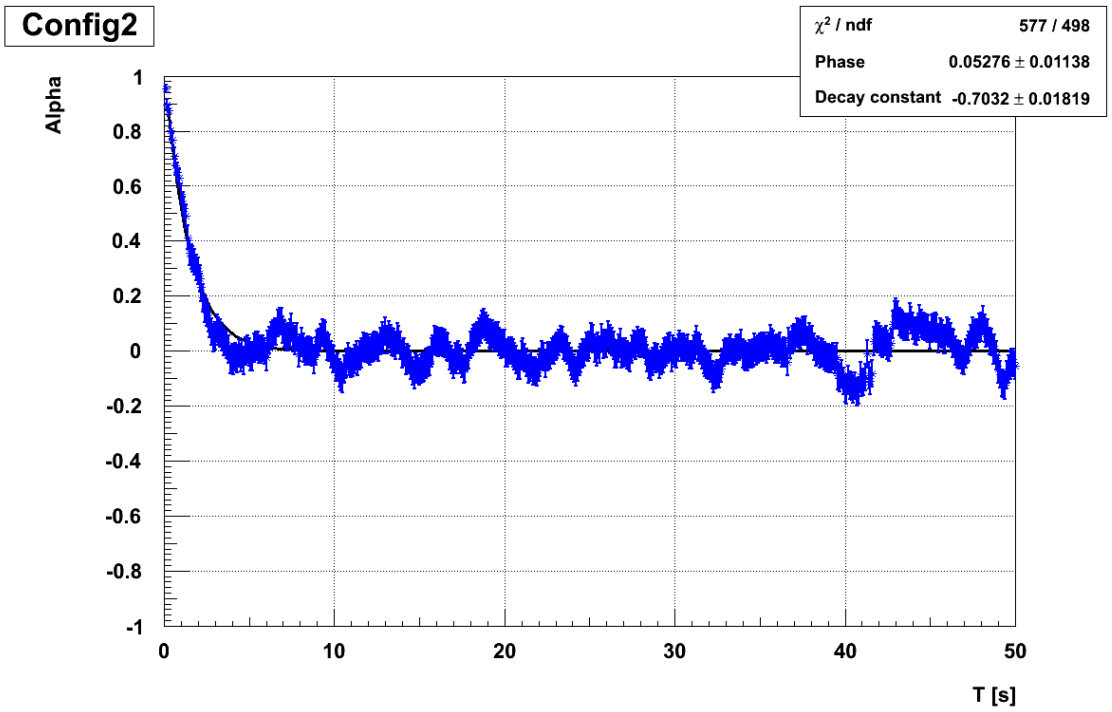

Figure 4.12: This plot shows the output of a simulation of neutrons within the base magnetic field as measured at ILL with no correction coils applied with their spins initially completely polarised in the plane perpendicular to B_z. The blue points plot the value of α, given in 4.13, the polarisation, as a function of time as the polarisation rapidly drops off as the neutrons (shown in 4.11) rapidly fall out of phase with rotating magnetic field. Alpha is here fitted to a single exponential to determine the decay constant, which gives the value of $T_2 \approx 2$s and demonstrates how poor the magnetic field inside the SCV is as this would mean that neutrons could not be stored for more than a couple of seconds before they become completely depolarised.

T_2 is computed by fitting this plot against an exponential of the form 4.10.

The results of the simulation for all the coil configurations measured are given in Fig. 4.13, showing both the simulated values of T_2 for the experimentally measured field taken at ILL and also for the 'predicted' field, which was produced by the field optimisation program by taking the coil configuration and the table of coil responses to predict what the coils would do to the field. Fig 4.13 shows this prediction to be relatively close to the experimentally produced field.

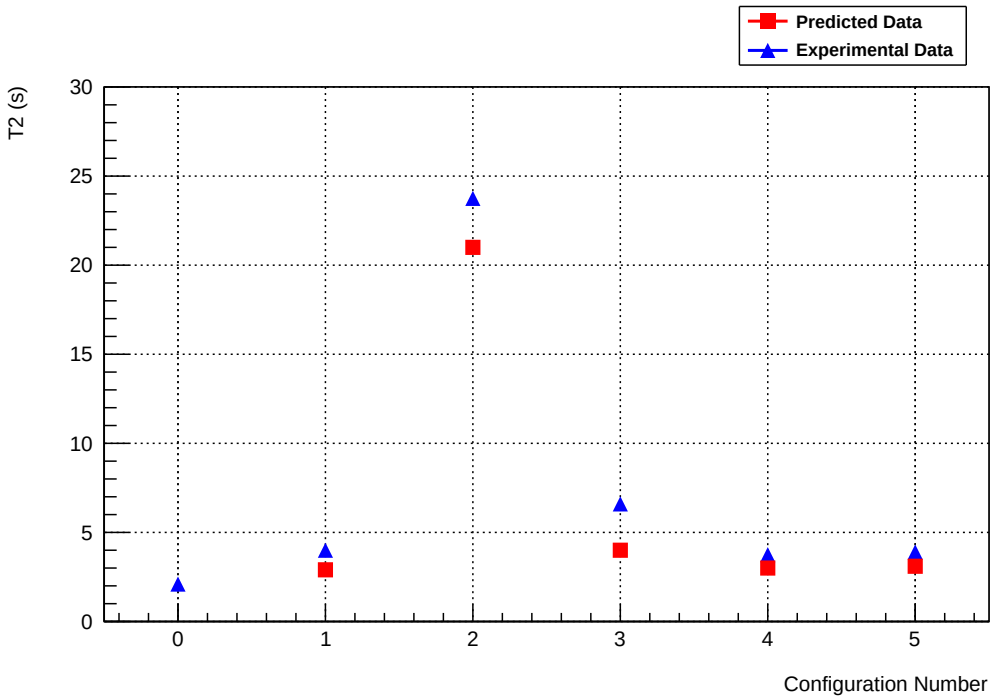

Figure 4.13: This shows the predicted value of T_2 as produced by the Monte Carlo simulation for all of the coil configurations in table 4.1. The blue points are the results of simulating T_2 against the experimentally measured data taken at the ILL with the coil configurations applied, while the red points are the results of simulating T_2 against predicted field-maps produced by the optimisation program, using the table of coil responses to predict what the field would be in a region for a particular current. The values of T_2 for both the measured and the predicted fields show reasonable agreement. Configuration 2 shows by far the biggest improvement in T_2 over the 'base' field.

This suggests that the only configuration to significantly improve T_2 was Config. 2, which is a largely hand-fit configuration, with relatively few free parameters. The base field configuration had a T_2 of roughly 2s, so the best configuration gave approximately an order of magnitude improvement in predicted T_2

However, unfortunately, Configuration 4, in which we optimised with all parameters free did not produce a significant improvement in T_2, suggesting that our model of the field uniformity, or, our χ^2 in Eq. 4.4, is not as related to T_2 as we originally assumed.

4.6.3 Optimising T_2 Directly

In the previous section we found that our previous attempts at optimising the field against a simple χ^2 function that tries to minimise the variation in the field as a proxy for optimising against T_2, largely failed.

For the immediate future, we did manage to find a set of compensation coil currents (Configuration 2) that provided a order of magnitude improvement in the predicted T_2 for the current generation SCV, raising the predicted T_2 to 20s. This would be enough to begin starting to try and observe a Rabi and possibly Ramsey resonance with the present apparatus.

However, clearly the long-term solution for the CryoEDM experiment is to investigate and try to remove the large magnetic-inclusions first, hopefully improving the magnetic field inhomogeneities observed in section 4.3 by at least an order of magnitude and then, repeating the work discussed here to attempt to gain *another* order of magnitude improvement in T_2 by using the compensation coils.

The CryoEDM collaboration has already begun carrying out work to both build a new, non-magnetic SCV and in the near future are working to isolate and remove the magnetic inclusions in the current SCV and baseplates.

To assist this effort, in this section we will discuss the feasibility of adapting this work in the future to try to optimise against T_2 directly; i.e: replacing the simple χ^2-function with a simulation to find T_2. To do this, however, we cannot solve the problem analytically as we did above, but must instead use a numerical minimisation routine, to gradually search the parameter space to find the optimum T_2.

4.6.3.1 Future Work: Optimising using the Minuit2 Framework

Minuit (`http://seal.web.cern.ch/seal/work-packages/mathlib/minuit/`) is a software library for performing numerical function minimisation, originally written in the Fortran programming language roughly 25 years ago, and has since been completely re-implemented in C++ under the name Minuit2. It is a large project, with a number of different minimisation strategies you can choose to fit your problem, as well as options such as putting constraints on parameters.

In order to optimise against T_2 we need to combine the Monte-Carlo simulation and its analysis functions that calculate a value for T_2, with the optimisation algorithms of Minuit2. To wrap the simulation inside of the optimisation process, we would need to boil the simulation and analysis of the simulation results down into a single function object that could be passed to Minuit.

That function would have to do a lot, and would be called on every iteration of the Minuit optimisation algorithm, potentially thousands, tens of thousands of times.

Currently a single simulation of 10000 neutrons can be at least ten minutes in length, if not more, for 100s of simulated neutron time. This would make such an optimisation prohibitively time consuming to get any sort of comprehensive global minima.

Thus, the workflow shown in Fig. 4.14 would need to be significantly optimised to be used in this way. Some suggested changes to be made would be,

1. *Eliminate I/O to disk* Reading and writing data structures out to disk, such as the generated field-map, and the particle simulation output, could be eliminated by keeping these data in memory for

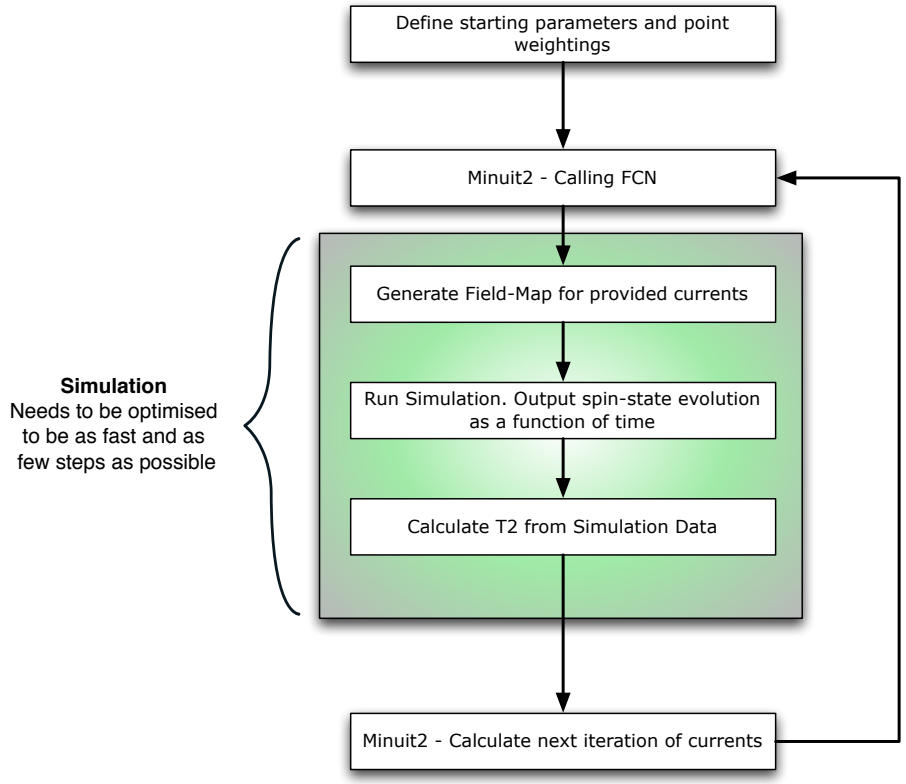

Figure 4.14: Flowchart depicting the steps required in a Minuit-based optimisation and showing the number of steps required to be performed for each stage of the optimisation. This would require a significant rewrite of certain parts of the simulation and require a lot of work to make things as fast as possible.

the whole calculation or until they are needed. For the kind of simulations needed, this shouldn't be a problem for the amount of RAM in modern computers.

2. *Simulate particles concurrently* Currently each particle is simulated individually for the entire time and then the next particle is simulated. If instead the simulation is changed so that each particle is simulated only until the next spin measurement, then at each spin measurement we can compute α as we go, rather than waiting until the entire simulation has finished to compute α as a function of time. The benefit here would be that we could attempt to extract T_2 by fitting the α plot after each spin measurement, and when the fit is 'good enough' we can exit the simulation early, without having to propagate every particle through the entire run time. In many cases we could likely produce a prety good fit after quite a short period of time, and thus would save vital simulation time.

3. *Multi-threading* This would be a significant, and technically challenging under-taking, however may be worth the effort if the need is great enough. If the effort is made to simulate particles concurrently, then it may make it easier to introduce threading to the simulation code, and thus particle's could be simulated in their own thread. This kind of simulation, where the particles are essentially non-interacting is an ideal candidate for multi-threading, and may lead to significant gains in performance.

As can be seen, there is a significant amount of work required to optimise the simulation to be used in this way. However, it is certainly possible should the need for another magnetic optimisation scan be great enough.

4.7 Summary of Findings

To conclude this chapter we will summarise our findings:

1. The current stainless steel SCV and it's baseplates have some residual magnetic inclusion(s) that significantly impact the holding, 5μT magnetic field, resulting in a gradient, $\partial B_z/\partial z$ across the ramsey cell region of order 300nT/m, compared to an design specification of just a few $O(1)$nT/m.

2. The magnetic inclusions do not appear to be affected by temperature, and we observe a similar field gradient, and qualitative field deformity at helium temperatures as we do at room temperatures.

3. The base holding field has a predicted T_2 relaxation time of just $\approx$ 2s, computed using the Monte-Carlo simulation of neutron spins in one of the ramsey cells.

4. A thorough scan of the response of each individual compensation coil, as a function of current applied, across the ramsey cell region of the SCV has been performed. This data has been used to construct an optimisation algorithm that attempts to find the optimum set of compensation coil currents that will minimise the variation in the base magnetic field across the ramsey cell region.

5. Work on attempting to optimise the magnetic field resulted, fortuitously, in a configuration of coils that lead to an order of magnitude improvement in T_2, up to over 20s. However, unfortunately the current configuration produced by a free fit from the optimisation routine did not produce a significant improvement in T_2 suggesting that our routine fails to properly optimise for our parameter of interest.

5 Conclusion

The main work of this thesis has been to outline a new monte-carlo based simulation for ultra-cold neutrons within the CryoEDM experiment. As shown in Chapter 3, the simulation was designed from the start specifically for UCN physics and is capable of tracking the motion of UCN as they propagate under gravity through 3-dimensional geometries of arbitrary complexity. The simulation also includes the major interactions of UCN with material containers, such as absorption and inelastic upscattering, as well as the interaction of neutron spin with static magnetic fields of arbitrary complexity.

The simulation has also been used by the author to study the results of a separate piece of work, outlined in chapter 4. This work involved carrying out a full magnetic scan, at low temperature, of the Ramsey cell region of the experiment to characterise inhomogeneities in the holding magnetic field due to impurities in the super-fluid containment vessel. Using this information, a process was developed to find an optimal set of currents for a set of 19 coils around the experiment's measurement chamber, so as to minimise magnetic gradients across the measurement cell. The author wrote a seperate, new piece of software to run this analysis with and produced 4 sets of coil currents, with different constraints placed on each.

The monte-carlo simulation was then used to analyse the potential impact of these coil configurations on the T_2 spin relaxation time. The simulation showed that we could potentially see an order of magnitude

improvement in T_2 by using the best of the coil configurations, taking T_2 from 2s to 20s.

Potential Future Developments

There are a number of areas of the simulation in need of greater testing and improvement to enable new kinds of studies. One is to test and improve the implementation of the electric field interaction with neutrons, specifically the $\vec{v} \times \vec{E}$ effect, outlined in [13]. This effect introduces an additional phase difference due to the motion of UCN through the electric field, appearing to the neutron as an additional magnetic field that can shift it's precession frequency and appear as a false EDM, which is one of the main systematic errors of CryoEDM.

The simulation also currently doesn't have a good solution for time-varying geometries, for example, opening of valves and flaps such as those around the detector in CryoEDM. In the simulation currently, a valve has been implemented that only has two positions, fully open and fully shut. For each state of the valve, a new simulation must be run, with the results of the previous simulation providing the input to the next. It would be nice to implement this process in a such a way that it could happen within a single simulation.

Improvements to the scattering process could also be investigated. Currently the diffuse scattering parameter acts only to mark a fixed percentage of all reflections on a surface as being diffuse. A good improvement would be to look more deeply at the physics here and base this parameter on a physical quality that could hopefully be measured for different materials.

Bibliography

[1] N. F. Ramsey, "Electric-dipole moments of elementary particles," *Reports on Progress in Physics*, vol. 45, no. 1, p. 95, 1982.

[2] J. Donoghue, E. Golowich, and B. Holstein, *Dynamics of the Standard Model*. Cambridge University Press, 1994.

[3] J. Smith, E. Purcell, and N. Ramsey, "Experimental Limit to the Electric Dipole Moment of the Neutron," *Physical Review*, vol. 108, no. 120, 1957.

[4] C. Baker, Y. Chibane, M. Chouder, P. Geltenbort, K. Green, P. G. Harris, B. R. Heckel, P. Iaydjiev, S. N. Ivanov, I. Kilvington, S. K. Lamoreaux, D. J. May, J. M. Pendlebury, J. D. Richardson, D. B. Shiers, K. F. Smith, and M. V. D. Grinten, "Apparatus for measurement of the electric dipole moment of the neutron using a cohabiting atomic-mercury magnetometer," *Nuclear Instruments and Methods in Physics Research Section A: Accelerators, Spectrometers, Detectors and Associated Equipment*, vol. 736, pp. 184–203, 2014.

[5] M. Pospelov and A. Ritz, "Neutron EDM from Electric and Chromoelectric Dipole Moments of Quarks," *Physical Review D*, vol. 63, no. 073015, 2001.

[6] R. Golub, D. Richardson, and S. Lamoreaux, *Ultra Cold Neutrons*. CRC Press, 1991.

[7] R. Golub and J. Pendlebury, "Ultra-Cold Neutrons," *Reports on Progress in Physics*, vol. 42, no. 439, 1979.

[8] V. Ignatovich, *The Physics of Ultracold Neutrons*. Oxford Science Publications, 1990.

[9] M. Goldberger and F. Seitz, "Theory of the refraction and the diffraction of neutrons by crystals," *Physical Review*, vol. 71, no. 5, pp. 294–310, 1947.

[10] A. Dianoux and G. Lander, *Neutron Data Booklet*. OCP Science, 2003.

[11] K. Nakamura, "Review of Particle Physics," *Journal of Physics G: Nuclear and Particle Physics*, vol. 37, no. 075021, 2010.

[12] R. Golub and J. Pendlebury, "Super-thermal sources of ultra-cold neutrons," *Physics Letters A*, vol. 53, no. 2, pp. 133–135, 1975.

[13] J. Pendlebury, W. Heil, Y. Sobolev, P. Harris, J. Richardson, R. Baskin, D. Doyle, P. Geltenbort, K. Green, M. van der Grinten, P. Iaydjiev, S. Ivanov, D. May, and K. Smith, "Geometric-phase-induced false electric dipole moment signals for particles in traps," *Physical Review A*, vol. 70, p. 032102, Sept. 2004.

[14] M. van der Grinten, "CryoEDM: A cryogenic experiment to measure the neutron electric dipole moment," *Nuclear Instruments and Methods in Physics Research Section A: Accelerators, Spectrometers, Detectors and Associated Equipment*, vol. 611, pp. 129–132, Dec. 2009.

[15] J. Pendlebury and D. Richardson, "Effects of gravity on the storage of ultracold neutrons," *Nuclear Instruments and Methods in Physics Research Section A: Accelerators, Spectrometers, Detec-*

tors and Associated Equipment, vol. 337, no. 2-3, pp. 504–511, 1994.

[16] J. R. Grozier, *Neutron Electric Dipole Moment Experiment : Magnetic Challenges and Solutions*. PhD thesis, University of Sussex, 2007.

[17] N. F. Ramsey, "Feasibility of a 3He magnetometer for neutron electric dipole moment experiments," *Acta Physica Hungarica*, vol. 55, no. 1-4, pp. 117–126, 1984.